Cell

Article

Biofilm formation on human immune cells is a multicellular predation strategy of *Vibrio cholerae*

Graphical abstract

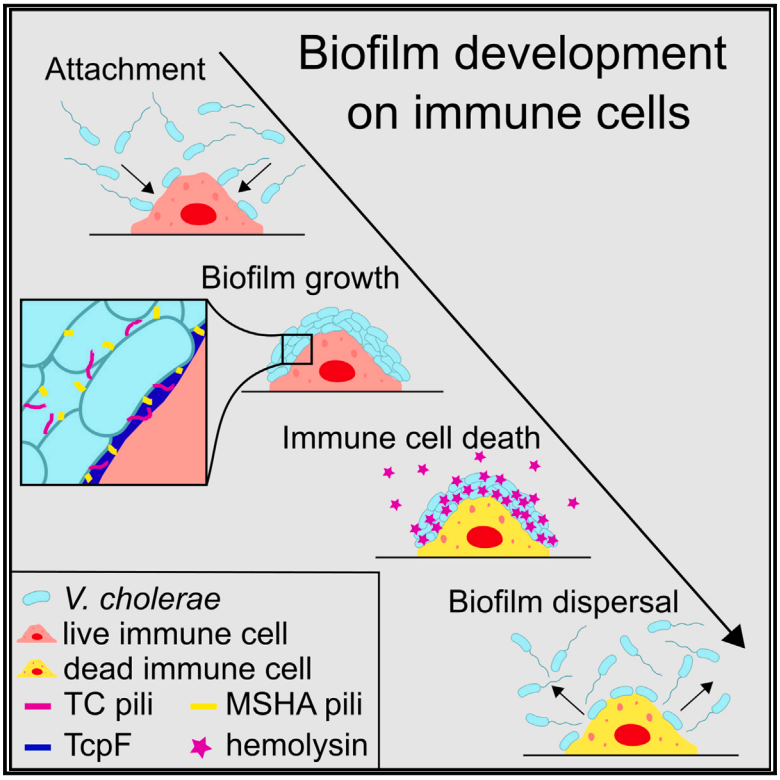

Authors

Lucia Vidakovic, Sofya Mikhaleva, Hannah Jeckel, ..., Alexandre Persat, Roi Avraham, Knut Drescher

Correspondence

knut.drescher@unibas.ch

In brief

For the human pathogen *Vibrio cholerae*, biofilm formation is not only a protective trait but also an aggressive trait where biofilms form on immune cells, encase and kill them, and then disperse.

Highlights

- *Vibrio cholerae* encases different types of immune cells by forming biofilms on them
- The biofilm matrix on immune cells differs from the matrix on other surfaces
- Biofilm formation enhances the delivery of the toxin hemolysin to kill immune cells
- Biofilm formation on immune cells is an aggressive multicellular bacterial trait

Vidakovic et al., 2023, Cell *186*, 2690–2704
June 8, 2023
https://doi.org/10.1016/j.cell.2023.05.008

CellPress

CellPress
OPEN ACCESS

Cell

Article

Biofilm formation on human immune cells is a multicellular predation strategy of *Vibrio cholerae*

Lucia Vidakovic,[1] Sofya Mikhaleva,[2,11] Hannah Jeckel,[1,3,11] Valerya Nisnevich,[4,11] Kerstin Strenger,[1,11] Konstantin Neuhaus,[1,3] Keerthana Raveendran,[5] Noa Bossel Ben-Moshe,[4] Marina Aznaourova,[6] Kazuki Nosho,[1] Antje Drescher,[1] Bernd Schmeck,[6,7,8,9,10] Leon N. Schulte,[6,9] Alexandre Persat,[2] Roi Avraham,[4] and Knut Drescher[1,12,*]

[1]Biozentrum, University of Basel, 4056 Basel, Switzerland
[2]Institute of Bioengineering and Global Health Institute, School of Life Sciences, École Polytechnique Fédérale de Lausanne, 1015 Lausanne, Switzerland
[3]Department of Physics, Philipps-Universität Marburg, 35043 Marburg, Germany
[4]Department of Immunology and Regenerative Biology, Weizmann Institute of Science, 7610001 Rehovot, Israel
[5]Max Planck Institute for Terrestrial Microbiology, 35043 Marburg, Germany
[6]Institute for Lung Research, Center for Synthetic Microbiology (SYNMIKRO), Universities of Giessen and Marburg Lung Center, Philipps-Universität Marburg, 35043 Marburg, Germany
[7]Department of Pulmonary and Critical Care Medicine, University Medical Center Marburg, 35043 Marburg, Germany
[8]German Center for Infection Research (DZIF), 35043 Marburg, Germany
[9]German Center for Lung Research (DZL), 35043 Marburg, Germany
[10]Institute for Lung Health, 35392 Giessen, Germany
[11]These authors contributed equally
[12]Lead contact
*Correspondence: knut.drescher@unibas.ch
https://doi.org/10.1016/j.cell.2023.05.008

SUMMARY

Biofilm formation is generally recognized as a bacterial defense mechanism against environmental threats, including antibiotics, bacteriophages, and leukocytes of the human immune system. Here, we show that for the human pathogen *Vibrio cholerae*, biofilm formation is not only a protective trait but also an aggressive trait to collectively predate different immune cells. We find that *V. cholerae* forms biofilms on the eukaryotic cell surface using an extracellular matrix comprising primarily mannose-sensitive hemagglutinin pili, toxin-coregulated pili, and the secreted colonization factor TcpF, which differs from the matrix composition of biofilms on other surfaces. These biofilms encase immune cells and establish a high local concentration of a secreted hemolysin to kill the immune cells before the biofilms disperse in a c-di-GMP-dependent manner. Together, these results uncover how bacteria employ biofilm formation as a multicellular strategy to invert the typical relationship between human immune cells as the hunters and bacteria as the hunted.

INTRODUCTION

In the environment, bacteria are frequently confronted by a wide range of predators, including bacteriophages, other bacterial species, and eukaryotes. Interactions between bacteria and their predators shape microbial populations, and predation is recognized as the main cause of bacterial mortality.[1–3] As a consequence of the continuous arms race between bacteria and their predators, bacteria have evolved sophisticated defense mechanisms to avoid being killed. Besides single-cell strategies, such as classical bacteriophage defense systems or immune evasion systems, bacteria can act collectively to protect themselves from predation through the formation of biofilms.[4–8]

Biofilms can serve as a protective refuge for bacteria because the extracellular biofilm matrix establishes a barrier that prevents the infiltration of the community by bacteriophages and predatory bacteria.[9–11] Biofilms also enable bacteria to escape the immune system of human hosts by impeding bacterial recognition or by reducing proinflammatory responses.[12–16] In addition, the increased size of the biofilm communities compared with solitary cells results in a grazing resistance of biofilms against phagocytosis by leukocytes.[17] Furthermore, biofilm-dwelling cells are highly tolerant against antibiotics,[18,19] which provides an additional facet to the protective nature of biofilms during human infections. Biofilm formation during human infections is an important adaptation for bacteria, as evidenced by the frequent emergence of biofilm matrix-overproducing mutants during long-term infections and by the fact that bacteria can respond to the presence of immune cells by forming biofilms.[20–23] Beyond the documented protective aspects of biofilms during

infections, the scope and mechanisms of interactions between biofilms and the immune system are unclear.

To investigate the interactions between biofilms and the immune system, we used human leukocytes and the bacterium *Vibrio cholerae* (*V. cholerae*), which is a model organism for biofilm research and the causative agent of the diarrheal disease cholera.[24–26] During human infection, *V. cholerae* colonizes the small intestine, resulting in disruptions of the epithelium and the establishment of an inflammatory response.[27–30] Upon induction of the immune response, different types of immune cells infiltrate the site of infection, which can result in a direct interaction of these immune cells with *V. cholerae*.[27–33] To evade clearance by neutrophils, *V. cholerae* has been shown to produce several toxins that together contribute to bacterial survival in the small intestine.[34] How *V. cholerae* interacts with immune cells on the cellular level, and whether biofilms have a function in this interaction, is unknown.

By studying the interaction of *V. cholerae* and immune cells, we discovered an unexpected process: *V. cholerae* forms biofilms on the surface of human immune cells and kills the immune cells, which is followed by biofilm dispersal. We revealed the mechanisms underlying this interaction process for macrophages and show that biofilms enhance killing of the immune cells by establishing a high concentration of a particular toxin near the leukocyte surface. Biofilm formation is therefore not only a collective protection mechanism from immune cells but also a mechanism for collective predation of immune cells.

RESULTS

V. cholerae forms biofilms on different human immune cells

To explore the interaction between cells of the innate and adaptive immune system and *V. cholerae*, we isolated neutrophils, $CD4^+$ T cells, natural killer (NK) cells, B cells, and $CD14^+$ monocytes from human blood, and we differentiated $CD14^+$ monocytes into macrophages. When exposing these human immune cells to wild-type (WT) *V. cholerae*, we observed that the bacterial cells quickly attached to the immune cell surface. Bacteria then accumulated over time and colonized the entire immune cell surface by forming a thick multicellular layer (Figure 1A). After a few hours of encapsulation by the bacterial layer, the immune cells died, followed by bacterial dispersal. The dynamics of bacterial accumulation on immune cells and dispersal are reflected by microscopy-based measurements of the volume of attached bacteria per volume of an annulus around each of the immune cells in the field of view (Figure 1B). We found that *V. cholerae* displayed this interaction process not only with macrophages differentiated from primary $CD14^+$ monocytes (Figures 1A and 1B) but also with macrophages differentiated from the monocytic cell line THP-1 (Figure 1C). Interestingly, *V. cholerae* displayed a much stronger attachment to macrophages compared with monocytes for both peripheral blood-derived cells (Figure S1A) and the THP-1 cell line (Figure 1D), indicating that this interaction process is specific. A proteomic comparison between macrophages and monocytes revealed numerous potential bacterial binding partners on the macrophage surface (Table S1), which were further investigated with pull-down experiments that are described in the section on the biofilm matrix composition below. Given that *V. cholerae* displayed similar interaction dynamics for the various immune cells, we performed a comprehensive analysis of the mechanisms and functions of this interaction process using THP-1-derived macrophages as a representative example, and we confirmed key results using primary macrophages. In addition, we used a co-culture infection model with macrophages, enteroid monolayers, and *V. cholerae* to study the interaction of *V. cholerae* with macrophages.

To determine whether the thick bacterial layer on macrophages primarily results from continuous attachment of planktonic bacteria or from bacterial cell division on the macrophage surface, we tracked the origin of each new bacterial cell on the macrophage surface using live-cell microscopy at single-cell resolution. We found that after an initial period with a high rate of bacterial attachment by planktonic bacteria, cell division takes over to dominate the process of accumulation into a multi-cell-layer structure on the macrophages (Figure 1E). The importance of bacterial growth for the accumulation on macrophages was further corroborated by measurements of the interaction process with a different multiplicity of infection (MOI): initiating the co-incubation process with a reduced number of bacterial cells at a fixed number of macrophages did not change the interaction outcome qualitatively, but it did result in a delayed accumulation of bacteria on macrophages (Figure S2A). Keeping the bacterial count constant for a different seeding number of macrophages did not change the interaction outcome significantly (Figure S2B). Given that the three-dimensional bacterial structures attached to the macrophage surface are primarily formed by bacterial cell division rather than cell aggregation and given that they consist of multiple bacterial cell layers, which implies the presence of an extracellular matrix that binds cells together (characterized further below), we consider these structures formed by *V. cholerae* on the surface of macrophages to be biofilms.

Analogous to the biofilm life cycle on abiotic surfaces, the biofilm development process we observed on immune cells (Figure 1) incorporates attachment, growth into 3D structures, and dispersal. We first sought to understand the key mechanisms underlying these three developmental stages, and if they differ from biofilm development on other surfaces, before characterizing the functions of biofilms on macrophages.

Attachment to macrophages is enabled by flagella, motility, and two different type IV pili

To understand how *V. cholerae* establishes the close interaction with human macrophages, we used RNA sequencing (RNA-seq) to perform time-resolved measurements of the bacterial transcriptomes during co-incubation. Data analysis revealed progressing transcriptional changes in *V. cholerae* for all four biological replicates, with 1,577 genes being significantly upregulated over the course of the interaction process (Figures S2F and S2G). Among those, we identified genes responsible for production of the flagellum and different type IV pili, which are the competence pilus, mannose-sensitive hemagglutinin (MSHA) pilus, and toxin-coregulated (TC) pilus (Figure 2A). In addition, genes coding for several other proteins that facilitate attachment of *V. cholerae* to biotic and abiotic surfaces[35,36] show a

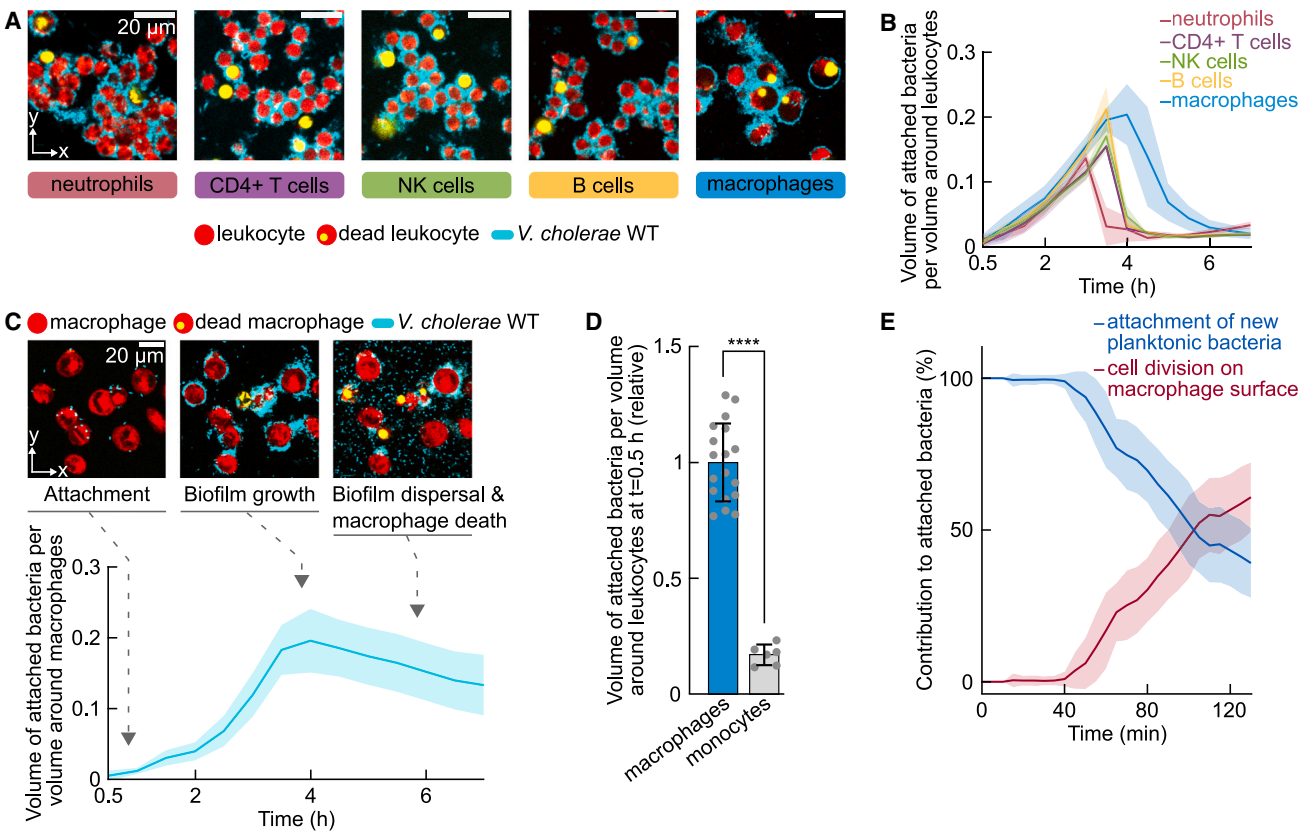

Figure 1. *V. cholerae* forms biofilms on human leukocytes, which is followed by immune cell death and biofilm dispersal

(A) *V. cholerae* cells attach to different types of human leukocytes isolated from blood and form biofilms before the leukocytes die and bacteria disperse collectively from the immune cell surface. Confocal microscopy images were acquired with a 40× NA 1.3 objective and show xy slices of *V. cholerae* (cyan) attached to leukocytes (red) at the time of peak number of attached bacterial cells shown in (B). Dead leukocytes are shown in yellow.

(B) Bacterial attachment to leukocytes was measured from confocal images: lines represent the mean ratio of the volume of attached bacteria per volume of an annulus around each immune cell; shaded regions denote the standard deviation of n independent biological replicates ($n_{macrophages}$ = 17; $n_{neutrophils}$ = 5; $n_{CD4+\ T\ cells}$ = 3; $n_{NK\ cells}$ = 3; $n_{B\ cells}$ = 3).

(C) *V. cholerae* cells also form biofilms on macrophages derived from the monocytic THP-1 cell line, followed by biofilm dispersal and macrophage cell death. Confocal images from different time points show distinct stages of the interaction process. Dead staining (yellow, propidium iodide) reveals an increasing number of dead macrophages over time. Bacterial attachment to macrophages was measured from confocal images: the solid line indicates the mean ratio of the volume of attached bacteria per volume of an annulus around each macrophage; the shaded region corresponds to the standard deviation of n = 41 independent biological replicates.

(D) Attachment of *V. cholerae* to the eukaryotic surface is strongly reduced for THP-1 monocytes, compared with THP-1-derived macrophages, measured after 30 min of co-incubation. Bars denote mean values; error bars denote the standard deviation of n independent biological replicates ($n_{macrophages}$ = 18; $n_{monocytes}$ = 6). Statistical significance was calculated using an unpaired t test (**** indicates $p < 0.001$). Similar results were obtained when comparing *V. cholerae* attachment to macrophages and monocytes derived from human blood (Figure S1A).

(E) Quantification of bacterial accumulation on the macrophage surface, which results either from the attachment of new planktonic cells or from the division of bacteria that are already attached to the macrophage surface. Macrophages were derived from THP-1 monocytes. Lines denote mean values; shaded areas are the standard deviation of n = 16 independent biological replicates.

differential expression profile. Based on our transcriptome data, we hypothesized that these factors are responsible for attachment of *V. cholerae* to macrophage surfaces.

However, deletion mutants for each of these factors revealed that only flagella and MSHA pili are essential for attachment to macrophages within the first hour of co-incubation (Figure 2B). The adhesins Mam7, GbpA, OmpU, and FrhA, which are known to be important for attachment to epithelial cells,[35] are not required for macrophage binding (Figure 2B). Ectopic expression of *mshA* or *flaA* under control of the native promoter restored bacterial attachment. Stalling the flagellar motor by the addition of phenamil also resulted in attenuated attachment, but the effect was not as strong as for the flagella deletion mutant, indicating that both the flagellar structure and cellular motility enabled by flagellar rotation contribute to attachment on macrophages. We confirmed that these findings from THP-1-derived macrophages are also true for primary $CD14^+$-derived macrophages (Figure S1B). Surprisingly, extended co-incubation revealed that Δ*mshA* cells can also attach to macrophages after a few hours, depending on the presence of the TC pilus with its major pilin TcpA and the secreted diffusive protein TcpF (Figure 2C), which is consistent with the expression dynamics of the

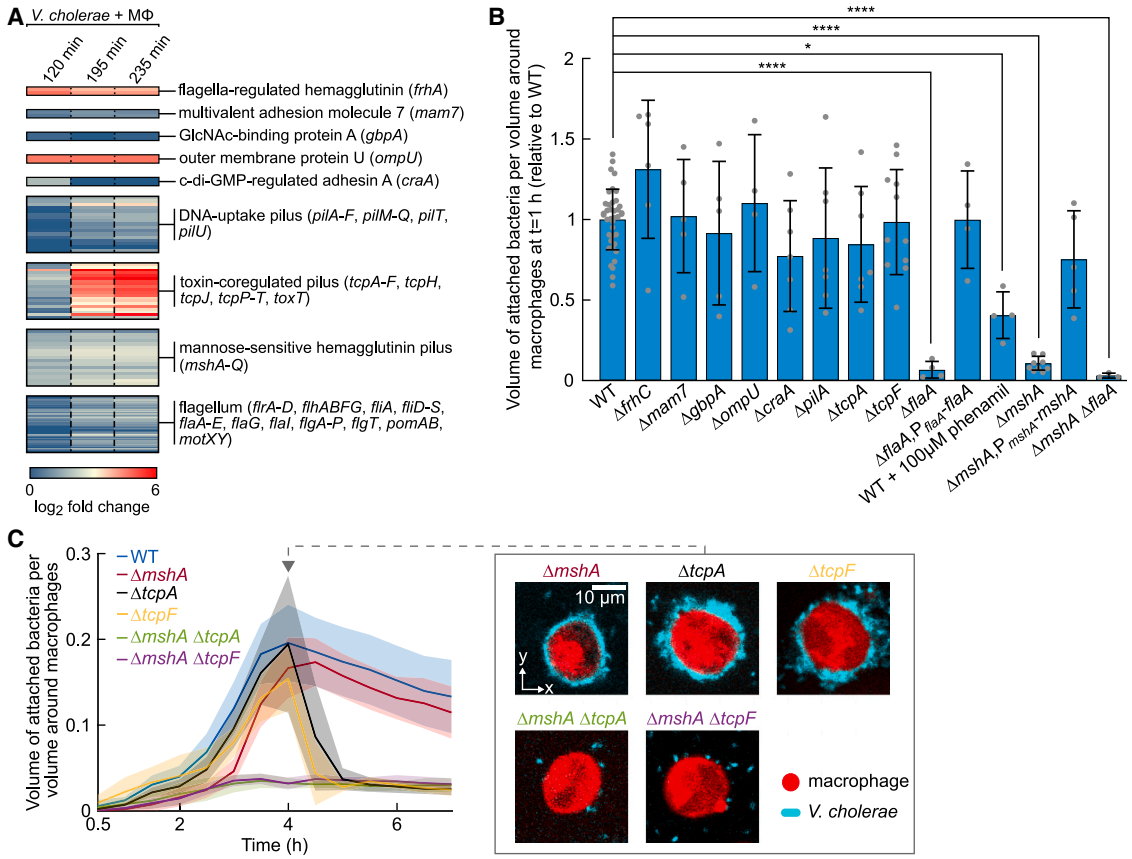

Figure 2. Attachment of *V. cholerae* to the surface of macrophages is enabled by type IV pili

(A) At different time points during co-incubation of bacteria and macrophages (Mφ), transcriptional changes of *V. cholerae* attached to macrophages were measured using RNA-seq. The heatmap shows expression dynamics of bacterial factors that are known to be involved in attachment of *V. cholerae* to different surfaces. Log_2 fold change values for the different time points were calculated relative to the bacterial sample taken at 0 min, prior to macrophage exposure. Values are the mean of n = 4 independent biological replicates.

(B) Quantification of bacterial attachment to macrophages after 1 h of co-incubation with *V. cholerae* deletion mutants that lack genes required for attachment to different surfaces. Bacteria deficient in the assembly of MSHA pili (Δ*mshA*) or the polar flagellum (Δ*flaA*), as well as cells with a stalled flagellar rotor (caused by the addition of 100 μM phenamil), exhibit impaired attachment to the macrophage surface. Ectopic expression of *mshA* or *flaA*, under the control of the native promoter, restores bacterial attachment. Mutants lacking other surface structures or proteins display attachment levels similar to WT bacteria. Bars represent the mean ratio of the volume of attached bacteria per volume of an annulus around each macrophage, after normalization to the mean value calculated for WT bacteria. Error bars denote the standard deviation of n = 3–39 independent biological replicates. Statistical analysis was performed using a one-way ANOVA (**** indicates $p < 0.0001$; * indicates $p < 0.02$).

(C) *V. cholerae* cells unable to produce MSHA pili (Δ*mshA*) eventually adhere to macrophages after prolonged co-incubation, which is dependent on TC pili and the secreted protein TcpF. The presence of either TC pili (with TcpF) or MSHA pili is sufficient for biofilm formation. Lines represent the mean ratio of the volume of attached bacteria per volume of an annulus around each macrophage at each time point. Shaded areas denote the standard deviation of n independent biological replicates ($n_{WT} = 41$; $n_{\Delta mshA} = 13$; $n_{\Delta mshA\ \Delta tcpA} = 17$; $n_{\Delta mshA\ \Delta tcpF} = 5$). Representative confocal images (xy slices) show bacterial accumulation (cyan) on the surface of macrophages (red) for different bacterial strains at the indicated time point.

tcp operon (Figure 2A). Correspondingly, expressing TC pili and TcpF earlier during co-incubation results in earlier attachment to macrophages (Figure S3A). Therefore, *V. cholerae* attachment to macrophage surfaces requires either flagella and MSHA pili or flagella and TC pili together with TcpF.

Biofilm matrix composition on macrophages differs from matrix on other surfaces

Biofilm growth into a 3D structure with multiple cell layers requires cell-cell binding, which typically involves an extracellular matrix. On abiotic surfaces, several matrix components of *V. cholerae* biofilms have been identified: the proteins Bap1, RbmA, and RbmC and the *Vibrio* polysaccharide (VPS).[37] Using immunofluorescence and a transcriptional reporter, we determined that these matrix components are also present in biofilms formed on macrophages but at low levels (Figures S3C–S3F): the matrix proteins encased only a few bacterial cells, mostly located at the outer edge of the biofilms, and a low fluorescence signal from the *vps* transcriptional reporter was present throughout the biofilms. However, on macrophages, we observed that bacteria lacking all of these components can still form biofilms that are similar to WT biofilms (Figure 3A), even

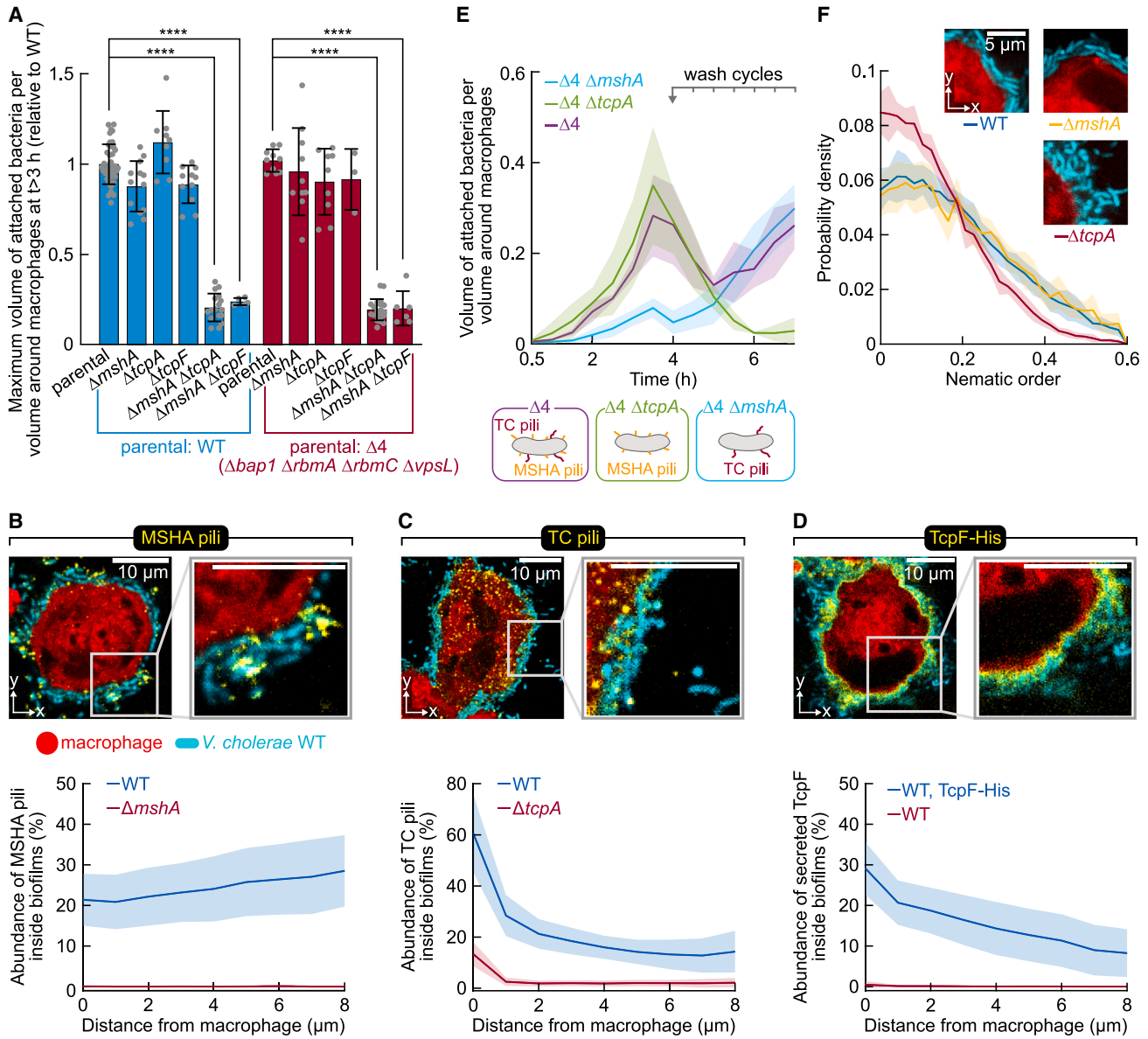

Figure 3. The extracellular matrix of biofilms formed on macrophages consists of MSHA pili, TC pili, and TcpF, which provide different biofilm functions

(A) *V. cholerae* biofilm growth on the surface of macrophages requires the production of MSHA pili or TC pili (together with TcpF) but does not depend on matrix components that are essential for biofilms formed on abiotic surfaces: Bap1, RbmA, RbmC, and VPS. Bars represent the mean ratio of the volume of attached bacteria per volume of an annulus around each macrophage at the time of peak biofilm accumulation. Attachment values are normalized to the WT mean value. Error bars indicate the standard deviation of n = 3–41 independent biological replicates. Statistical significance was calculated using one-way ANOVA (**** indicates $p < 0.0001$).

(B–D) Localization and abundance of MSHA pili (B), TC pili (C), and TcpF (D) inside the biofilm formed on macrophages, measured after 4 h of co-incubation. Microscopy images show *V. cholerae* biofilms (cyan) on macrophages (red) and a specific biofilm matrix component (yellow, immunofluorescence) at the peak time of bacterial biomass accumulation. Graphs show the spatial distribution of MSHA pili, TC pili, and TcpF inside the biofilm. MSHA pili are present throughout the biofilm, but TC pili and the secreted protein TcpF predominantly localize close to the surface of macrophages. Lines represent the mean abundance of a matrix component inside biofilms; shaded areas are the standard deviation of biofilms formed on a number of X macrophage cells ($X_{WT;MSHA\ pili}$ = 41; $X_{\Delta mshA;MSHA\ pili}$ = 15; $X_{WT;TC\ pili}$ = 19; $X_{\Delta tcpA;TC\ pili}$ = 31; $X_{TcpF\text{-}His;TcpF}$ = 26; $X_{TcpF;TcpF}$ = 36), from n = 3 independent biological replicates.

(E) Production of TC pili provides mechanical stability to biofilms: repeated medium exchange during the *V. cholerae*-macrophage interaction dynamics resulted in continuous removal of biofilms that lack TC pili from the macrophage surface. "Δ4" denotes the mutations Δ*bap1* Δ*rbmA* Δ*rbmC* Δ*vpsL*. Lines denote the mean values; shaded areas are the standard deviation of n independent biological replicates ($n_{\Delta4}$ = 3; $n_{\Delta4\ \Delta tcpA}$ = 3; $n_{\Delta4\ \Delta mshA}$ = 3).

(F) Production of TC pili affects biofilm compactness: single-cell resolution analysis of the biofilm architecture revealed that Δ*tcpA* mutants produce biofilms with a lower cell-cell alignment, measured in terms of the distribution of the nematic order parameter. WT and Δ*mshA* biofilms display a similar cell-cell alignment.

(legend continued on next page)

though this mutant is incapable of biofilm formation on abiotic surfaces.[37]

Instead of relying on these well-known matrix components, we found that biofilm growth on macrophages requires the production of at least one of the two type IV pili: MSHA pili or TC pili (Figures 3A and S1C). Furthermore, biofilm growth via TC pili relies on the presence of TcpF (Figures 3A and S1C). As shown above, these two pili structures are required for attachment of *V. cholerae* to macrophages (Figure 2), yet the pili are also extracellular structures that could potentially act as extracellular matrix components. To test whether MSHA pili and TC pili are part of the extracellular matrix, we directly visualized and quantified MSHA pili, TC pili, and TcpF via immunofluorescence and found that they are indeed present in biofilms on macrophages (Figures 3B–3D). While MSHA pili were localized uniformly across the entire biofilm (Figure 3B), TC pili and the secreted protein TcpF were predominantly found near the macrophage surface (Figures 3C and 3D). The *V. cholerae* biofilm matrix on macrophages therefore relies on a different set of components compared with the biofilm matrix on other surfaces.

To investigate the interaction between TC pili and TcpF, we performed experiments with purified TcpF, which was exogenously supplied to a bacterial strain overexpressing TC pili, in a Δ*mshA* Δ*tcpF* background. Overexpression of the *tcp* operon was achieved by overexpressing the transcriptional activator ToxT. These experiments revealed that the presence of TC pili alone is not sufficient for bacterial biofilm formation on macrophages (Figure S3B). However, when purified TcpF was added exogenously, biofilm formation of this bacterial strain on macrophages increased in a TcpF concentration-dependent manner. These results suggest that *V. cholerae* uses TC pili to bind to the protein TcpF, while TcpF interacts directly with the eukaryotic surface (Figure 3D), which explains our observation that TC pili and TcpF act together, as shown in Figures 2C, 3A, S3A, and S3B.

To uncover the binding partners on the macrophage surface for the key biofilm matrix components, we used our proteomic differential abundance analysis of macrophages and monocytes (Table S1) and additionally performed pull-down experiments with MshA or TcpF as bait and macrophage lysate as prey, followed by liquid chromatography-mass spectrometry (LC-MS) analysis. For MSHA pili, we identified 22 potential binding partners on the macrophage surface (which are not found on monocytes), 12 of which are glycoproteins; in the case of TcpF, we found 36 potential protein binding partners on the macrophage surface (Tables S2 and S3).

Given that we determined that MSHA pili and TC pili are part of the biofilm matrix on macrophages, they might confer different properties to the biofilm. An analysis of the mechanical stability of biofilms on macrophages revealed that the presence of TC pili enabled *V. cholerae* biofilms to better withstand mechanical stress (Figure 3E). In addition, an analysis of the biofilm architecture on macrophages revealed that TC pili contribute to the establishment of a high cell-cell alignment inside *V. cholerae* biofilms on macrophages (Figure 3F). Because the production of one type of pilus, either MSHA pili or TC pili, is already sufficient for attachment to macrophages (Figures 2C, S3A, and S3B) and for biofilm formation on macrophages (Figures 2C and 3A), our data show that both type IV pili are engaged in bacteria-bacteria interactions as well as bacteria-immune cell interactions.

Biofilm dispersal on macrophages relies on TC pili and c-di-GMP reduction

Biofilm dispersal is the final stage of biofilm development on macrophages, which requires the cells to disengage from the biofilm matrix to enable their departure. To understand the key mechanisms underlying biofilm dispersal from macrophages, we investigated the different matrix components during dispersal. We observed not only that the presence of TC pili influences the stability and structure of biofilms as described above (Figures 3E and 3F) but that TC pili also determine the extent of biofilm dispersal. Biofilms lacking TC pili (Δ*tcpA*) displayed stronger dispersal than the parental strain, and biofilms in which the *tcp* operon was overexpressed displayed reduced dispersal (Figure 4A). Biofilms lacking MSHA pili displayed similar dispersal capabilities to the parental strain (Figure 4A). These data suggest that the regulation of TC pili production is essential for biofilm dispersal.

Consistent with this hypothesis, the transcriptome data during the *V. cholerae*-macrophage interaction show that the *tcp* operon is indeed downregulated during dispersal (Figure 4B). During the late stage of *V. cholerae* infection in humans and in animal models, *tcp* is also downregulated,[38,39] which may enable dispersal not only from epithelial cells[39] but also from immune cells. The transcript levels of the *msh* operon are unaffected by dispersal (Figure 4B), which is consistent with the finding that the lack of MSHA does not affect biofilm dispersal (Figure 4A).

For biofilms grown on abiotic surfaces, a decrease in the intracellular levels of the second messenger signaling molecule c-di-GMP is known to regulate the transition between biofilm formation and dispersal for several species.[40] We therefore speculated that a reduction of c-di-GMP levels may also cause *V. cholerae* biofilm dispersal from the macrophage surface. We tested this idea by first measuring c-di-GMP levels during biofilm growth and dispersal using a reporter for c-di-GMP levels based on an unstable fluorescent protein reporter. These measurements revealed that biofilm dispersal coincided with a reduction in c-di-GMP levels (Figure 4C). To test whether a step decrease in c-di-GMP levels causes biofilm dispersal, we grew biofilms on macrophages until just before dispersal would have occurred naturally and then induced the expression of two c-di-GMP-degrading phosphodiesterases (RocS and CdgJ). We found that biofilms dispersed directly after overexpression of the two phosphodiesterases, whereas biofilms of the empty vector control continued to grow and dispersed later (Figure 4D). Together, the results from Figure 4 demonstrate that, on macrophage surfaces, biofilm dispersal requires a regulation of TC pili and that dispersal is controlled by intracellular c-di-GMP levels.

Representative confocal microscopy images show biofilms of different bacterial strains on macrophages (macrophages in red, bacteria in cyan). Lines denote mean values, and shaded areas are the standard deviation of biofilms formed on a number of X macrophages (X_{WT} = 10; $X_{\Delta mshA}$ = 7; $X_{\Delta tcpA}$ = 9) from n = 3 independent biological replicates.

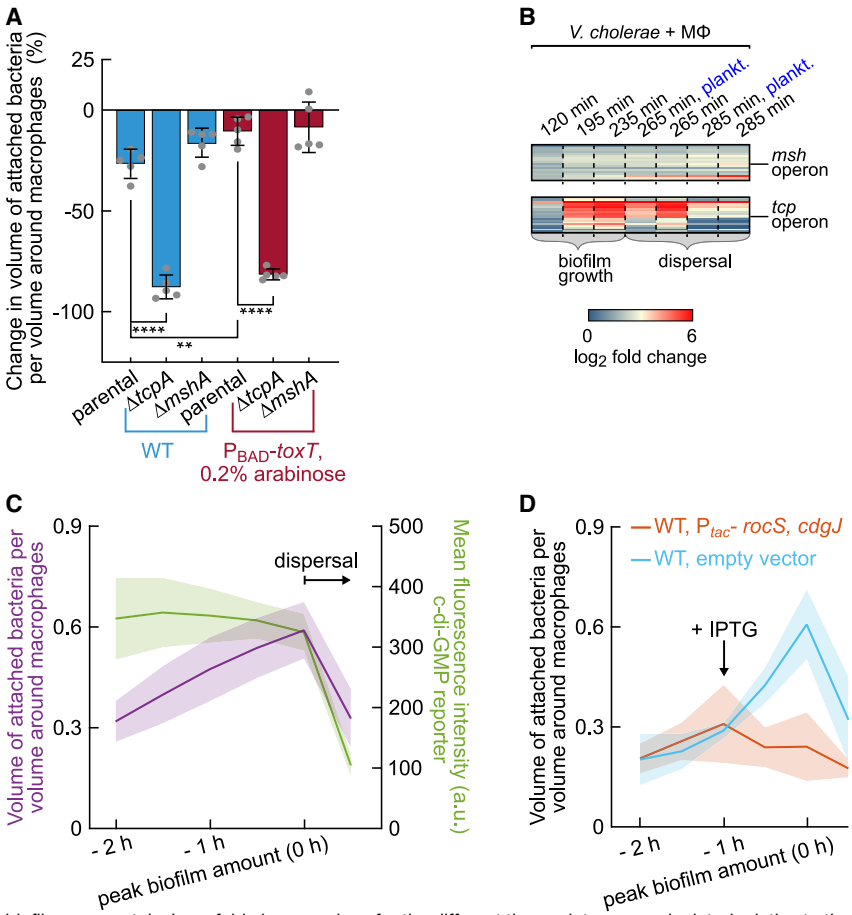

Figure 4. Biofilm dispersal is determined by intracellular c-di-GMP levels and the presence of TC pili

(A) The presence of TC pili in the biofilm matrix of *V. cholerae* biofilms impacts biofilm dispersal from the macrophage surface. Biofilm dispersal from macrophages was quantified as the difference between the attached bacterial biovolume at the time of peak biofilm formation and 1 h later. The attached bacterial biovolume was measured as the ratio of the volume of attached bacteria per volume of an annulus around each macrophage. Biofilm dispersal is significantly lower for WT biofilms compared with biofilms formed by Δ*tcpA* cells. Overexpression of *toxT* under control of the arabinose-inducible promoter P_{BAD} further reduces the degree of biofilm dispersal, which is dependent on the presence of TC pili. For biofilms lacking MSHA pili, the level of dispersal was comparable to the respective parental strain. Bars represent the mean values. Error bars denote the standard deviation of n = 5 independent biological replicates. Statistical significance was calculated using one-way ANOVA or an unpaired t test (**** indicates $p < 0.0001$; ** indicates $p < 0.01$).

(B) Analysis of the *V. cholerae* transcriptome dynamics during the interaction with macrophages reveals that genes encoding TC pili are upregulated during biofilm growth. Initiation of biofilm dispersal coincides with the downregulation of the *tcp* operon. Genes encoding MSHA pili are not differentially expressed in the transition between biofilm growth and dispersal. For the two time points that included dispersed bacteria (t = 265 min and t = 285 min), RNA-seq was performed for planktonic cells and bacteria still residing in biofilms separately. Log_2 fold change values for the different time points were calculated relative to the bacterial sample taken at 0 min. Values are the mean of n = 4 independent biological replicates.

(C) Measurement of intracellular c-di-GMP levels using a fluorescent reporter (based on an unstable GFP, green line) during biofilm growth and dispersal and simultaneous measurement of the attached bacteria per macrophage (purple line). Biofilm dispersal coincides with a decrease in c-di-GMP reporter fluorescence. Lines represent mean values, and shaded areas indicate the standard deviation of n = 3 independent biological replicates.

(D) Induced overexpression of the two c-di-GMP-degrading phosphodiesterases RocS and CdgJ under control of the IPTG-inducible P_{tac} promoter causes biofilm dispersal (orange line). *V. cholerae* biofilms harboring the empty vector (negative control; blue line) continue to grow on the macrophage surface despite the addition of IPTG until bacteria naturally disperse from the macrophage surface. Lines denote the mean level of attached bacteria per macrophage; shaded areas indicate the standard deviation of n = 3 independent biological replicates.

Biofilms around macrophages enhance macrophage killing by increasing toxin delivery

After identifying the key processes for bacterial attachment, biofilm formation, and biofilm dispersal on macrophages as described above, we set out to investigate the functional benefits that *V. cholerae* derives from biofilm formation on macrophages. We first hypothesized that the thick biofilms and their pilus-based matrix might impede inflammatory signaling by limiting the diffusion of the cytokines through the biofilm. However, measurements of secreted cytokine levels showed that *V. cholerae* biofilms on macrophages did not interfere with the release of these signals into the environment (Figure S2H).

Alternatively, we hypothesized that thick biofilms around macrophages may contribute to macrophage killing (Figures 1A and 1C). In support of this hypothesis, we found that biofilm thickness on macrophages correlates with macrophage death (Figure 5A). We therefore investigated how *V. cholerae* kills macrophages and how biofilms are involved in this process.

V. cholerae encodes many hypothetical and known toxins, of which several displayed differential transcription changes during co-incubation with macrophages (Figure 5B). To test their contribution to macrophage death, we generated deletion mutants lacking each one of the potential killing factors. Exposure to macrophages for 7 h revealed that *V. cholerae* lacking the toxin HlyA causes significantly less macrophage death compared to WT bacteria. Deletions of other toxins did not result in significant differences compared to WT bacteria (Figure 5C). The hemolysin HlyA is a pore-forming toxin that is secreted in a monomeric form but oligomerizes in host cell membranes and induces cell lysis.[41–44] Overexpression of HlyA restored the phenotype and caused increased macrophage death (Figure 5C). We also confirmed that HlyA induces cell death for macrophages derived from monocytes isolated from human blood (Figure S1D). Further deletion of toxin-encoding genes in the Δ*hlyA* background strain did not significantly change the macrophage death rate compared to Δ*hlyA* cells (Figure S4). We also observed that

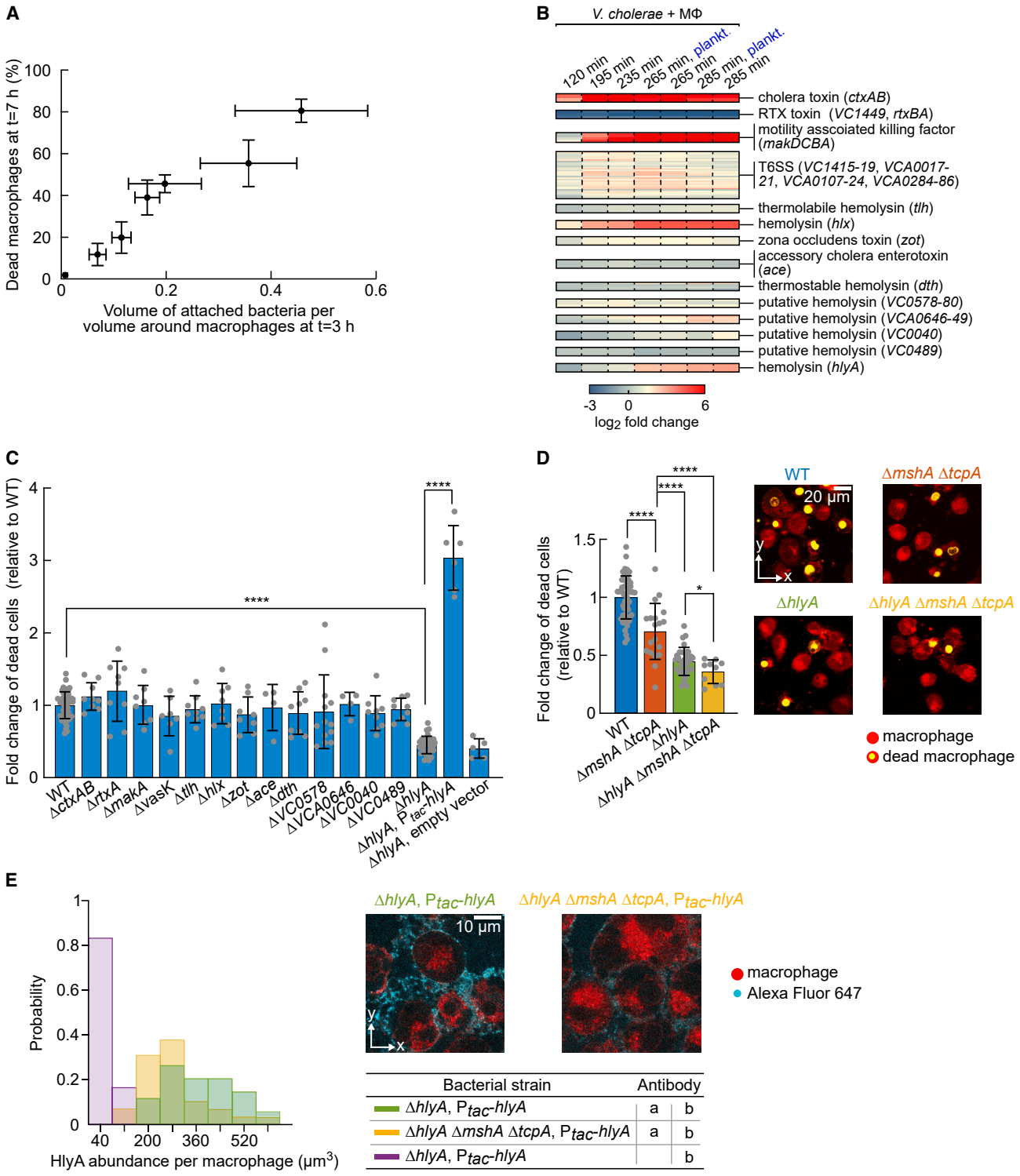

Figure 5. Encapsulation of macrophages by bacterial biofilms increases cell death of macrophages

(A) The fraction of dead macrophages increases with increased *V. cholerae* WT biofilm amount on the immune cell surface. As a metric for the amount of biofilm, we measured the volume of attached bacteria per volume of an annulus around macrophages after 3 h of co-incubation, and we counted dead macrophages after 7 h of co-incubation (n = 3–52 independent biological replicates, error bars denote the standard deviation).

(B) RNA-seq measurements were performed at different time points during the co-incubation of *V. cholerae* with THP-1-derived macrophages (Mφ). Transcriptomic analysis shows that genes encoding known and putative toxins and the type VI secretion system (T6SS) in *V. cholerae* were differentially expressed

(legend continued on next page)

an increased MOI led to an increased macrophage death (Figure S2C). Together, these results establish that *V. cholerae* uses HlyA as the major toxin for killing macrophages.

To test whether the biofilm around the macrophages contributes to the HlyA-dependent killing of macrophages, we exposed macrophages to bacteria that cannot form biofilms on macrophages (Δ*mshA* Δ*tcpA*) and monitored the occurrence of macrophage death using microscopy and propidium iodide staining. Bacteria deficient in biofilm formation (Δ*mshA* Δ*tcpA*) induced significantly less macrophage death than WT bacteria (Figure 5D). For monocytes, where we observed a reduction in bacterial attachment compared to macrophages (Figure 1D), we also observed a reduction in cell death (Figure S2E). Additional deletion of the hemolysin (Δ*mshA* Δ*tcpA* Δ*hlyA*) caused a further reduction in macrophage death (Figure 5D), indicating that the hemolysin and the biofilm structure both contribute to macrophage killing. We also confirmed the importance of biofilms for HlyA-based macrophage killing, using macrophages derived from monocytes isolated from human blood (Figure S1E).

As biofilm formation and hemolysin production both impact the viability of macrophages, we wanted to understand how these two factors of the *V. cholerae*-macrophage interaction affect the response of macrophages toward bacterial encounters. Exposure of macrophages to WT, biofilm-deficient, or hemolysin-deficient *V. cholerae* strains followed by RNA-seq revealed that each of these *V. cholerae* strains induces similar changes in the macrophage transcriptome compared to untreated macrophages (Figure S2I). Therefore, biofilm growth and hemolysin production do not contribute to the transcriptional response in macrophages observed during the encounter with *V. cholerae*, despite the fact that both traits significantly contribute to death of macrophages.

To understand how biofilms contribute to the HlyA-dependent macrophage killing, we determined the localization of secreted HlyA via immunofluorescence. In the presence of *V. cholerae* biofilms on macrophages, HlyA accumulates on and near the macrophage surface (Figure 5E). In contrast, secreted HlyA was significantly less abundant when macrophages were exposed to biofilm-deficient bacteria (Figure 5E). Biofilm formation on macrophages therefore enhances the ability of *V. cholerae* to kill the macrophages by establishing a high concentration of the secreted diffusible toxin HlyA near the macrophage surface.

As hemolysin forms pores in the host cell membrane that can lead to an uncontrolled egress of macrophage cellular contents, we sought to understand whether *V. cholerae* can utilize cellular components of macrophages for growth. Monitoring bacterial growth in the presence of lysate generated from macrophages revealed that *V. cholerae* displayed enhanced growth in a lysate-concentration-dependent manner (Figure S2D). The killing of macrophages is therefore a predatory trait of *V. cholerae*.

V. cholerae forms biofilms on macrophages after breaking through human enteroid monolayers

V. cholerae pathogenesis in the human small intestine relies on colonization of the intestinal epithelium.[45] This colonization leads to the infiltration of immune cells at the site of infection and disruptions of the epithelial barrier, which enable an interaction between bacteria and immune cells.[27–33,46] To investigate whether *V. cholerae* is able to form biofilms on immune cells after colonizing and breaking through the epithelium, we established a co-culture model with epithelial monolayers derived from human small intestinal organoids (enteroids) and macrophages. In this co-culture model, macrophages were cultured on the basal side of an enteroid monolayer that was differentiated on a permeable insert (Figure 6A). Infection was then initiated by adding bacteria to the apical side of the enteroid monolayer (Figure 6A). The interactions between bacteria, the epithelial barrier, and macrophages were monitored by time-lapse confocal microscopy. During infection, we observed colonization of enteroid monolayers by *V. cholerae* WT (Figure 6A) and a progressing disruption of the epithelial barrier integrity. After the epithelial barrier became compromised, bacteria reached the basal side and formed biofilms on macrophages (Figure 6A), similar to the process described in Figure 1. Using macrophages derived from monocytes that were isolated from human blood instead of THP-1-derived macrophages showed a similar progression of infection (Figure S5A). Using enteroids from different human donors resulted in similar interaction dynamics and biofilm formation on macrophages (Figures 6A and S6A).

Previous measurements of the bacterial load in the small intestine in a rabbit model of *V. cholerae* infection showed that there

during bacterial interaction with macrophages, particularly after longer co-incubation. At the two time points of co-incubation that included dispersing cells (t = 265 min, t = 285 min), RNA-seq was performed separately on the planktonic cells and the cells that remained in biofilms attached to macrophages. Log_2 fold change values for the different time points were calculated relative to the bacterial sample taken at 0 min. Values are the mean of n = 4 independent biological replicates.

(C) Macrophage death was measured using microscopy and propidium iodide staining after 7 h of co-incubation with *V. cholerae* strains that lack genes required for the production of known or putative toxins. In the presence of Δ*hlyA* bacteria, the occurrence of macrophage cell death is decreased compared to WT bacteria. Ectopic expression of *hlyA* under control of the P_{tac} promoter restored and even increased killing of macrophages. Bars represent the percentage of dead macrophages for different *V. cholerae* strains, normalized to the WT (n = 4–52 independent biological replicates, error bars denote the standard deviation). Statistical significance was calculated using one-way ANOVA (**** indicates $p < 0.0001$). Data for *V. cholerae* toxin double mutants are shown in Figure S4.

(D) Biofilm formation contributes to *V. cholerae*-induced macrophage death. Representative microscopy images show dead macrophages (yellow, propidium iodide staining) after 7 h exposure to particular *V. cholerae* strains. Bars represent the percentage of dead macrophages for different *V. cholerae* strains, normalized to the WT (n = 10–52 independent biological replicates, error bars denote the standard deviation). Statistical significance was calculated using a one-way ANOVA or an unpaired t test (**** indicates $p < 0.0001$; * indicates $p < 0.05$).

(E) Immunofluorescence staining of HlyA (cyan in representative confocal images) shows that biofilms establish a high HlyA toxin abundance near the macrophage surface compared to non-biofilm producing bacteria. Bars represent the probability for a particular HlyA abundance per macrophage for different conditions (described with the same color code in the table). Antibody treatments: "a," addition of mouse anti-HlyA antibody; "b," addition of anti-mouse Alexa Fluor 647 antibody. Number of imaged field of views that were analyzed: $N_{\Delta hlyA,\ Ptac\text{-}hlyA,\ a+b} = 38$, $N_{\Delta hlyA,\Delta mshA\ \Delta tcpA\ Ptac\text{-}hlyA,\ a+b} = 30$, $N_{\Delta hlyA,\ Ptac\text{-}hlyA,\ b} = 30$ from n = 3 independent biological replicates.

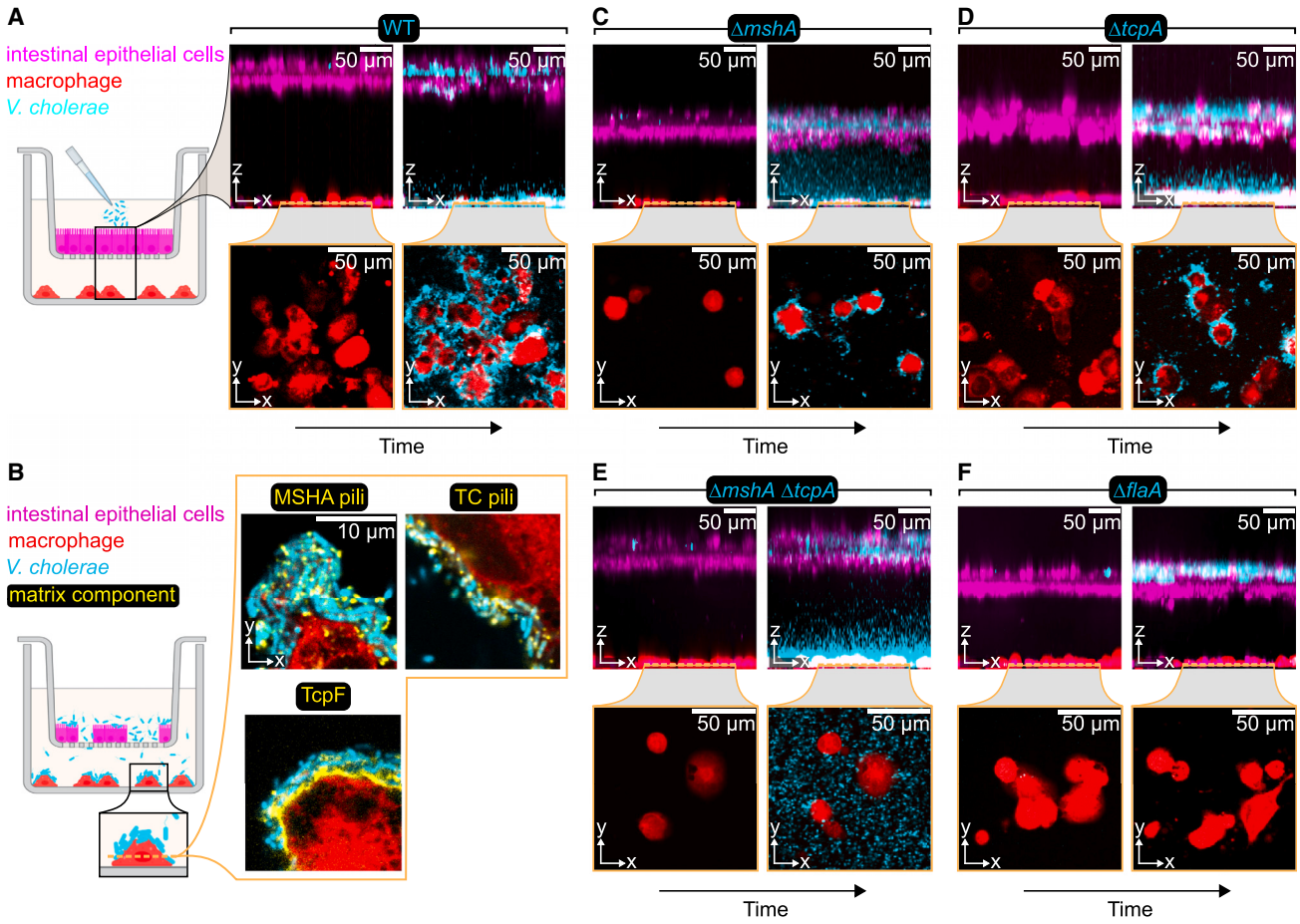

Figure 6. *V. cholerae* cells break the human intestinal epithelial barrier and subsequently form biofilms on macrophages underneath

(A) Differentiated human enteroid monolayers (donor #1) were grown on a permeable membrane insert (3 µm pore size) and placed above THP-1 macrophages as illustrated in the schematic diagram of the experimental setup. After adding *V. cholerae* to the apical side of the epithelium, bacteria grew and accumulated. Cell numbers at the start of infection: 3.2×10^6 bacteria, 9.1×10^4 epithelial cells, and 2.5×10^4 THP-1 macrophages. Different MOIs are shown in Figure S5B, results for primary macrophages are shown in Figure S5A, and results for enteroid monolayers from a different donor are shown in Figure S6. Over time, *V. cholerae* broke through the monolayer, reached the basal side, and formed biofilms on the macrophage surface. Representative confocal fluorescence images of n = 3 independent biological replicates show the xz side view (maximum projection) of enteroid monolayers, macrophages, and bacteria at the start of the co-culture and at the time of peak biofilm formation on macrophages (magenta: epithelial cells, red: macrophages, cyan: *V. cholerae*). For the same time points, xy images show the macrophages and *V. cholerae* biofilms underneath the epithelial cells.

(B) Visualization of MSHA pili, TC pili, and TcpF using fluorescently conjugated antibodies (shown in yellow) inside *V. cholerae* biofilms formed on macrophages during co-culture of enteroid monolayers, macrophages, and bacteria. Images are representative of n = 3 independent biological replicates.

(C–F) Co-culture of enteroid monolayers and macrophages infected with different *V. cholerae* mutants (mutations are indicated above each panel). Representative fluorescence images of n = 3 independent biological replicates show xz side views (maximum projection) and xy images in the same format as for (A). Images show the bacteria interaction with epithelial cells and macrophages at the start of co-culture and peak time of biofilm formation on macrophages (for C and D) or a time at which WT bacteria would have normally formed biofilms (for E and F). Results for additional mutants are shown in Figures S5C–S5F. Cell numbers at the start of infection: 3.2×10^6 bacteria, 9.1×10^4 epithelial cells, and 2.5×10^4 THP-1 macrophages.

are 10^5–10^9 bacterial cells per 0.3 cm^2 of luminal epithelial surface area.[47] Inspired by these measurements, we tested bacterial loads in the range of 3.2×10^5 to 6.4×10^6 bacteria per 0.33 cm^2 of intestinal epithelial surface in our co-culture model (Figure S5B). Exposing the epithelial monolayers to different cell numbers of *V. cholerae* WT showed that decreasing initial MOIs resulted in a delayed breaking of the enteroid monolayer, yet all initial MOIs eventually disrupted the epithelial barrier and led to biofilm formation on the macrophages underneath (Figure S5B).

The biofilms that formed on macrophages after breaking the enteroid monolayer also possess a matrix comprising MSHA pili, TC pili, and the secreted protein TcpF, as revealed by immunofluorescence (Figure 6B). An analysis of *V. cholerae* mutants in this co-culture model showed that strains lacking MSHA pili (Δ*mshA*), TC pili (Δ*tcpA*), or both (Δ*mshA* Δ*tcpA*) could attach to epithelial cells and break the epithelial barrier, but biofilm formation on the macrophages underneath required the presence of one of the two type IV pili (Figures 6C–6E, S5F, and S6), which is consistent with findings shown in Figures 2 and 3. Bacteria

lacking flagella (Δ*flaA*) did not reach the basal side of the enteroid monolayers and consequently did not form biofilms on macrophages underneath (Figures 6F and S6I). Cells that lacked cholera toxin (Δ*ctxAB*), hemolysin (Δ*hlyA*), or the canonical matrix components employed for biofilms on abiotic surfaces (Δ*bap1* Δ*rbmA* Δ*rbmC* Δ*vpsL*) were still able to break the enteroid monolayer and formed biofilms on macrophages (Figures S5C–S5E and S6D–S6F). The interaction process we observed for any of the bacterial mutants did not depend on the human enteroid donor (Figures S5 and S6).

Together, our infections of the enteroid-derived human gut model demonstrate that *V. cholerae* is able to form biofilms on macrophages with a pilus-based matrix after colonizing the intestinal epithelium and disrupting the epithelial barrier. While biofilm formation on macrophages strongly depends on MSHA pili and TC pili, bacteria are still able to attach and disrupt the intestinal epithelium in the absence of these pili.

DISCUSSION

Our study shows that *V. cholerae* forms biofilms on the surface of various human immune cells and encases the immune cells. We found that biofilm formation on immune cells occurs after breaching the epithelial barrier in our enteroid infection model. Furthermore, biofilm formation on immune cells is a widespread process, but not an untargeted process, as we observed this behavior for neutrophils, NK cells, $CD4^+$ T cells, B cells, and macrophages, but not for monocytes. Our analysis revealed two fundamental aspects of these biofilms: mechanisms controlling different stages of biofilm development on immune cells and the function of biofilms on immune cells.

Biofilm development on macrophages involves bacterial attachment, matrix production, and three-dimensional growth, as well as biofilm dispersal, which is qualitatively analogous to biofilm development on abiotic surfaces. However, we showed that the mechanisms involved in biofilm development on macrophages are different from those on other surfaces.

The biofilm matrix of *V. cholerae* on glass, agar, and chitin primarily consists of the polysaccharide VPS and the proteins RbmA, RbmC, and Bap1.[37] On intestinal epithelial cells, *V. cholerae* can form microaggregates in which the cells are bound together by TC pili.[48] In suspensions, *V. cholerae* is able auto-aggregate into multicellular clumps using the TC pilus and the DNA-uptake pilus,[49,50] which is a process that does not require bacterial growth. In contrast, we showed that biofilms grown on macrophages form a matrix that consists of MSHA pili, TP pili, and TcpF and that the canonical matrix components VPS, RbmA, RbmC, and Bap1 are dispensable. We speculate that type IV pili are convenient biofilm matrix components for *V. cholerae* during acute infection because these pili can be quickly assembled and retracted to potentially enable rapid rearrangement of the biofilm and dispersal. Utilizing different matrix components for biofilms in different environments is an interesting bacterial adaptation.

Beyond the differences in biofilm matrix composition, the mechanism of surface attachment is also different on macrophages compared with other surfaces. Attachment to glass and chitin surfaces involves flagella and MSHA pili.[51,52] Attachment to epithelial cells requires TC pili and TcpF, as well as the adhesins GbpA, FrhA, OmpU, and Mam7.[48,53–58] In contrast, we found that for the attachment of *V. cholerae* to macrophages, the adhesins GbpA, FrhA, OmpU, and Mam7 are irrelevant. Instead, the attachment to macrophages relies on flagella, bacterial motility, and at least one of the two type IV pili:MSHA pili or TC pili together with the secreted colonization factor TcpF. Bacterial strains lacking both pili (Δ*mshA* Δ*tcpA*) cannot attach to macrophages, yet they can attach to epithelial cells.

The function of biofilms on macrophages also differs from the prevailing interpretation of the function of biofilms on other surfaces. Biofilm formation often provides protection to the constituent cells by increasing their tolerance to stresses and by inhibiting access of predators to the bacterial population.[8,10,19,20,37,59] In contrast, we show that biofilm formation on macrophages enhances the killing of macrophages by establishing a locally high concentration of the secreted toxin HlyA around the macrophages. Interestingly, *V. cholerae* has been shown to evade eradication by neutrophils in a toxin-dependent manner in a mouse model,[34] and our study suggests that biofilm formation on those immune cells might be crucial for efficient toxin delivery. For *Pseudomonas aeruginosa* (*P. aeruginosa*), it has previously been observed that rhamnolipids, which are secreted by planktonic cells and by cells in biofilms, can kill immune cells, particularly when the immune cells actively move toward mature *P. aeruginosa* biofilms.[60–62] In contrast, our study shows that *V. cholerae* establishes a direct interaction with immune cells via biofilm formation on and around the immune cells, which ultimately results in the killing of the immune cells. Therefore, *V. cholerae* biofilm formation on and around immune cells and the biofilm-dependent enhanced toxin delivery to immune cells differ qualitatively from previously described interaction processes between bacteria and immune cells. Although many bacterial pathogens are able to form biofilms during infections, it remains to be investigated how widespread biofilm formation on immune cells is among other pathogens and whether biofilms on immune cells can have additional functions beyond enhancing toxin delivery and predation.

V. cholerae infection in humans elicits an inflammatory response that results in long-lasting immunity against subsequent infections.[29,63] Furthermore, anti-MSHA antibodies are found in the blood of cholera patients,[64] which has been a mystery so far because MSHA pili were not known to be involved in *V. cholerae* pathogenesis. In fact, *V. cholerae* needs to repress MSHA pili production during the early phase of intestinal colonization to avoid recognition by secretory IgA, the mucosal immune factor that binds to MSHA pili and thereby prevents bacterial penetration through the mucus layer and subsequent binding to epithelial cells.[65,66] Interaction studies of *V. cholerae* with epithelial cells and various animal models of *V. cholerae* infection have identified TC pili and TcpF as factors that act together during host colonization, yet the lack of MSHA pili did not affect the colonization ability.[48,53,54,67] Our data now reveal an important role of MSHA pili for attachment to immune cells and as part of the biofilm matrix on immune cells, which could explain the existence of anti-MSHA antibodies upon *V. cholerae* infection. Furthermore, our findings provide an additional facet to the importance of TC pili and TcpF during infections because of their involvement in the interaction with immune cells.

In conclusion, *V. cholerae* has developed a mechanism by which bacteria can act collectively to kill immune cells at the site of infection, which decreases the number of phagocytes in the surroundings. Consequently, *V. cholerae* does not use biofilm formation as a refuge in order to evade immune cells, as seen for other bacteria. Instead, *V. cholerae* employs biofilm formation as an aggressive multicellular strategy to predate immune cells.

Limitations of study

Although our results are consistent with known processes of *V. cholerae* infections in humans, and we observed *V. cholerae* biofilm formation on primary neutrophils, NK cells, $CD4^+$ T cells, and B cells isolated from human blood, as well as primary macrophages, and we observed that *V. cholerae* forms biofilms on macrophages after breaking through an enteroid monolayer at realistic MOIs, it is not possible to directly verify that biofilm formation on immune cells occurs during infections in humans.

V. cholerae is a human pathogen that does not normally infect other animals, yet animal models that reflect many of the features of human infections have been developed, based on mice and rabbits, where animals are treated with drugs[68,69] prior to exposure to *V. cholerae*. Although the immune system of mice and rabbits is different from humans,[70] studies of the late stages of *V. cholerae* infections in an animal model would be informative, yet such studies would still not directly test the role of biofilms on immune cells during human *V. cholerae* infection.

STAR★METHODS

Detailed methods are provided in the online version of this paper and include the following:

SUPPLEMENTAL INFORMATION

Supplemental information can be found online at https://doi.org/10.1016/j.cell.2023.05.008.

ACKNOWLEDGMENTS

We thank Karen Skorupski for generously providing us with the rabbit anti-TcpA6 antibody and Nils Schmerer for assistance during the isolation of leukocytes. We are also grateful to Fitnat H. Yildiz for advice and Sanika Vaidya, Daniel Rode, and Praveen K. Singh for strains, as well as Alexander Schmidt and Thomas K.C. Bock from the Proteomics Core Facility at the Biozentrum of the University of Basel. This research was enabled by grants from the Minna James Heineman Foundation (to K.D. and R.A.), the Deutsche Forschungsgemeinschaft (DR 982/5-1, DR 982/6-1, and SPP 2389), the European Union's Horizon 2020 research and innovation program through the European Research Council (grant agreement 716734), the Bundesministerium für Bildung und Forschung (TARGET-Biofilms 16GW0245), the Max Planck Society, the National Centre of Competence in Research AntiResist, funded by the Swiss National Science Foundation grant 51NF40_180541, and the Swiss National Science Foundation Consolidator Grant TMCG-3_213801 (to K.D.). S.M. is funded by a postdoc fellowship from the Peter und Traudl Engelhorn Stiftung zur Förderung der Lebenswissenschaften. H.J. is funded by the Studienstiftung des Deutschen Volkes and the Joachim Herz Foundation. A.P. is funded by the Human Frontier Science Program (RGY0077/2020) and the Swiss National Science Foundation (310030_204190). R.A. is supported by the Israel Science Foundation (grant No. 1289/22). B.S. and L.N.S. are funded by the Hessisches Ministerium für Wissenschaft und Kunst (LOEWE Diffusible Signals) and the Deutsche Forschungsgemeinschaft (SFB/TR-84 TP C01 and TP C10). B.S. is also funded by the German Ministry for Education and Research (BMBF) (ERACoSysMed2 SysMed-COPD-FKZ 031L0140 and Permed-COPD FKZ 01EK2203).

AUTHOR CONTRIBUTIONS

L.V. and K.D. conceived the project, designed experiments, and analyzed data. L.V., S.M., K.S., and K.R. performed microscopy experiments. L.V., K.S., and K.R. generated bacterial strains. S.M. and A.P. enabled the establishment of the co-culture model with human enteroid monolayers and macrophages. H.J. developed and L.V. performed image analysis. V.N., N.B.B.-M., L.N.S., and R.A. performed the transcriptome analysis. V.N., N.B.B.-M., and R.A. performed additional transcriptome measurements. K.S. performed proteomics experiments. K. Neuhaus developed microscope imaging techniques. K. Nosho, M.A., and L.N.S. contributed to RNA preparation for RNA sequencing. A.D., B.S., and L.S. provided human samples. L.V. and K.D. created the figures and wrote the manuscript with input from all authors. K.D. supervised and coordinated the project.

DECLARATION OF INTERESTS

All authors declare no competing interests.

INCLUSION AND DIVERSITY

We support inclusive, diverse, and equitable conduct of research.

Received: September 15, 2021
Revised: January 26, 2023
Accepted: May 9, 2023
Published: June 8, 2023

REFERENCES

1. Pernthaler, J. (2005). Predation on prokaryotes in the water column and its ecological implications. Nat. Rev. Microbiol. *3*, 537–546. https://doi.org/10.1038/nrmicro1180.
2. Pérez, J., Moraleda-Muñoz, A., Marcos-Torres, F.J., and Muñoz-Dorado, J. (2016). Bacterial predation: 75 years and counting. Environ. Microbiol. *18*, 766–779. https://doi.org/10.1111/1462-2920.13171.
3. Jürgens, K., and Matz, C. (2002). Predation as a shaping force for the phenotypic and genotypic composition of planktonic bacteria. Antonie Leeuwenhoek *81*, 413–434. https://doi.org/10.1023/A:1020505204959.
4. Rostøl, J.T., and Marraffini, L. (2019). Ph)ighting Phages: How Bacteria Resist Their Parasites. Cell Host Microbe *25*, 184–194. https://doi.org/10.1016/j.chom.2019.01.009.
5. Sarantis, H., and Grinstein, S. (2012). Subversion of phagocytosis for pathogen survival. Cell Host Microbe *12*, 419–431. https://doi.org/10.1016/j.chom.2012.09.001.
6. Arciola, C.R., Campoccia, D., and Montanaro, L. (2018). Implant infections: Adhesion, biofilm formation and immune evasion. Nat. Rev. Microbiol. *16*, 397–409. https://doi.org/10.1038/s41579-018-0019-y.
7. Matz, C., and Kjelleberg, S. (2005). Off the hook - How bacteria survive protozoan grazing. Trends Microbiol. *13*, 302–307. https://doi.org/10.1016/j.tim.2005.05.009.
8. Matz, C., McDougald, D., Moreno, A.M., Yung, P.Y., Yildiz, F.H., and Kjelleberg, S. (2005). Biofilm formation and phenotypic variation enhance predation-driven persistence of Vibrio cholerae. Proc. Natl. Acad. Sci. USA *102*, 16819–16824. https://doi.org/10.1073/pnas.0505350102.
9. Vidakovic, L., Singh, P.K., Hartmann, R., Nadell, C.D., and Drescher, K. (2018). Dynamic biofilm architecture confers individual and collective mechanisms of viral protection. Nat. Microbiol. *3*, 26–31. https://doi.org/10.1038/s41564-017-0050-1.
10. Wucher, B.R., Elsayed, M., Adelman, J.S., Kadouri, D.E., and Nadell, C.D. (2021). Bacterial predation transforms the landscape and community assembly of biofilms. Curr. Biol. *31*, 2643–2651.e3. https://doi.org/10.1016/j.cub.2021.03.036.
11. Díaz-Pascual, F., Hartmann, R., Lempp, M., Vidakovic, L., Song, B., Jeckel, H., Thormann, K.M., Yildiz, F.H., Dunkel, J., Link, H., et al. (2019). Breakdown of Vibrio cholerae biofilm architecture induced by antibiotics disrupts community barrier function. Nat. Microbiol. *4*, 2136–2145. https://doi.org/10.1038/s41564-019-0579-2.
12. Thurlow, L.R., Hanke, M.L., Fritz, T., Angle, A., Aldrich, A., Williams, S.H., Engebretsen, I.L., Bayles, K.W., Horswill, A.R., and Kielian, T. (2011). Staphyloccous auerus biofilms prevent marcophage pahgocytosis and attenuate inflammation in vivo. J. Immunol. *186*, 6585–6596. https://doi.org/10.4049/jimmunol.1002794.
13. Kristian, S.A., Birkenstock, T.A., Sauder, U., Mack, D., Götz, F., and Landmann, R. (2008). Biofilm formation induces C3a release and protects Staphylococcus epidermidis from IgG and complement deposition and from neutrophil-dependent killing. J. Infect. Dis. *197*, 1028–1035. https://doi.org/10.1086/528992.
14. Domenech, M., Ramos-Sevillano, E., García, E., Moscoso, M., and Yuste, J. (2013). Biofilm Formation Avoids Complement Immunity and Phagocytosis of Streptococcus pneumoniae. Infect. Immun. *81*, 2606–2615. https://doi.org/10.1128/IAI.00491-13.
15. Gunn, J.S., Bakaletz, L.O., and Wozniak, D.J. (2016). What's on the outside matters: The role of the extracellular polymeric substance of gram-negative biofilms in evading host immunity and as a target for therapeutic intervention. J. Biol. Chem. *291*, 12538–12546. https://doi.org/10.1074/jbc.R115.707547.
16. Mulcahy, L.R., Isabella, V.M., and Lewis, K. (2014). Pseudomonas aeruginosa Biofilms in Disease. Microb. Ecol. *68*, 1–12. https://doi.org/10.1007/s00248-013-0297-x.
17. Alhede, M., Lorenz, M., Fritz, B.G., Jensen, P.Ø., Ring, H.C., Bay, L., and Bjarnsholt, T. (2020). Bacterial aggregate size determines phagocytosis efficiency of polymorphonuclear leukocytes. Med. Microbiol. Immunol. *209*, 669–680. https://doi.org/10.1007/s00430-020-00691-1.
18. Yan, J., and Bassler, B.L. (2019). Surviving as a Community: Antibiotic Tolerance and Persistence in Bacterial Biofilms. Cell Host Microbe *26*, 15–21. https://doi.org/10.1016/j.chom.2019.06.002.
19. Høiby, N., Bjarnsholt, T., Givskov, M., Molin, S., and Ciofu, O. (2010). Antibiotic resistance of bacterial biofilms. Int. J. Antimicrob. Agents *35*, 322–332. https://doi.org/10.1016/j.ijantimicag.2009.12.011.
20. Hall-Stoodley, L., Costerton, J.W., and Stoodley, P. (2004). Bacterial biofilms: from the natural environment to infectious diseases. Nat. Rev. Microbiol. *2*, 95–108. https://doi.org/10.1038/nrmicro821.
21. Limoli, D.H., Jones, C.J., and Wozniak, D.J. (2015). Bacterial Extracellular Polysaccharides in Biofilm Formation and Function. Microbiol. Spectr. *3*. https://doi.org/10.1128/microbiolspec.MB-0011-2014.
22. Walker, T.S., Tomlin, K.L., Worthen, G.S., Poch, K.R., Lieber, J.G., Saavedra, M.T., Fessler, M.B., Malcolm, K.C., Vasil, M.L., Nick, J.A., et al. (2005). Enhanced Pseudomonas aeruginosa Biofilm Development Mediated by Human Neutrophils. Infect. Immun. *73*, 3693–3701. https://doi.org/10.1128/IAI.73.6.3693.
23. Chandra, J., McCormick, T.S., Imamura, Y., Mukherjee, P.K., and Ghannoum, M.A. (2007). Interaction of Candida albicans with adherent human peripheral blood mononuclear cells increases C. albicans biofilm formation and results in differential expression of pro- and anti-inflammatory cytokines. Infect. Immun. *75*, 2612–2620. https://doi.org/10.1128/IAI.01841-06.
24. Harris, J.B., LaRocque, R.C., Qadri, F., Ryan, E.T., and Calderwood, S.B. (2012). Cholera. Lancet *379*, 2466–2476. https://doi.org/10.1016/S0140-6736(12)60436-X.
25. Berk, V., Fong, J.C.N., Dempsey, G.T., Develioglu, O.N., Zhuang, X., Liphardt, J., Yildiz, F.H., and Chu, S. (2012). Molecular architecture and assembly principles of Vibrio cholerae biofilms. Science *337*, 236–239. https://doi.org/10.1126/science.1222981.
26. Hartmann, R., Singh, P.K., Pearce, P., Mok, R., Song, B., Díaz-Pascual, F., Dunkel, J., and Drescher, K. (2019). Emergence of three-dimensional order and structure in growing biofilms. Nat. Phys. *15*, 251–256. https://doi.org/10.1038/s41567-018-0356-9.
27. Mathan, M.M., Chandy, G., and Mathan, V.I. (1995). Ultrastructural changes in the upper small intestinal mucosa in patients with cholera. Gastroenterology *109*, 422–430. https://doi.org/10.1016/0016-5085(95)90329-1.
28. Qadri, F., Bhuiyan, T.R., Dutta, K.K., Raqib, R., Alam, M.S., Alam, N.H., Svennerholm, A.M., and Mathan, M.M. (2004). Acute dehydrating disease caused by Vibrio cholerae serogroups O1 and O139 induce increases in innate cells and inflammatory mediators at the mucosal surface of the gut. Gut *53*, 62–69. https://doi.org/10.1136/gut.53.1.62.
29. Weil, A.A., Becker, R.L., and Harris, J.B. (2019). Vibrio cholerae at the Intersection of Immunity and the Microbiome. mSphere *4*, e00597-19. https://doi.org/10.1128/mSphere.00597-19.
30. Flach, C.F., Qadri, F., Bhuiyan, T.R., Alam, N.H., Jennische, E., Lönnroth, I., and Holmgren, J. (2007). Broad up-regulation of innate defense factors during acute cholera. Infect. Immun. *75*, 2343–2350. https://doi.org/10.1128/IAI.01900-06.

31. Bishop, A.L., Patimalla, B., and Camilli, A. (2014). Vibrio cholerae-induced inflammation in the neonatal mouse cholera model. Infect. Immun. *82*, 2434–2447. https://doi.org/10.1128/IAI.00054-14.

32. Amadou Amani, S., and Lang, M.L. (2020). Bacteria That Cause Enteric Diseases Stimulate Distinct Humoral Immune Responses. Front. Immunol. *11*, 565648–565714. https://doi.org/10.3389/fimmu.2020.565648.

33. Seper, A., Hosseinzadeh, A., Gorkiewicz, G., Lichtenegger, S., Roier, S., Leitner, D.R., Röhm, M., Grutsch, A., Reidl, J., Urban, C.F., and Schild, S. (2013). Vibrio cholerae Evades Neutrophil Extracellular Traps by the Activity of Two Extracellular Nucleases. PLoS Pathog. *9*, e1003614. https://doi.org/10.1371/journal.ppat.1003614.

34. Queen, J., and Satchell, K.J.F. (2012). Neutrophils are essential for containment of Vibrio cholerae to the intestine during the proinflammatory phase of infection. Infect. Immun. *80*, 2905–2913. https://doi.org/10.1128/IAI.00356-12.

35. Almagro-Moreno, S., Pruss, K., and Taylor, R.K. (2015). Intestinal Colonization Dynamics of Vibrio cholerae. PLoS Pathog. *11*, e1004787. https://doi.org/10.1371/journal.ppat.1004787.

36. Kitts, G., Giglio, K.M., Zamorano-Sánchez, D., Park, J.H., Townsley, L., Cooley, R.B., Wucher, B.R., Klose, K.E., Nadell, C.D., Yildiz, F.H., et al. (2019). A conserved regulatory circuit controls large adhesins in vibrio cholerae. mBio *10*, 1–22. https://doi.org/10.1128/mBio.02822-19.

37. Teschler, J.K., Nadell, C.D., Drescher, K., and Yildiz, F.H. (2022). Mechanisms Underlying Vibrio cholerae Biofilm Formation and Dispersion. Annu. Rev. Microbiol. *76*, 503–532. https://doi.org/10.1146/annurev-micro-111021-053553.

38. LaRocque, R.C., Harris, J.B., Dziejman, M., Li, X., Khan, A.I., Faruque, A.S.G., Faruque, S.M., Nair, G.B., Ryan, E.T., Qadri, F., et al. (2005). Transcriptional profiling of Vibrio cholerae recovered directly from patient specimens during early and late stages of human infection. Infect. Immun. *73*, 4488–4493. https://doi.org/10.1128/IAI.73.8.4488-4493.2005.

39. Nielsen, A.T., Dolganov, N.A., Rasmussen, T., Otto, G., Miller, M.C., Felt, S.A., Torreilles, S., and Schoolnik, G.K. (2010). A bistable switch and anatomical site control vibrio cholerae virulence gene expression in the intestine. PLoS Pathog. *6*, e1001102. https://doi.org/10.1371/journal.ppat.1001102.

40. Jenal, U., Reinders, A., and Lori, C. (2017). Cyclic di-GMP: Second messenger extraordinaire. Nat. Rev. Microbiol. *15*, 271–284. https://doi.org/10.1038/nrmicro.2016.190.

41. Zitzer, A., Zitzer, O., Bhakdi, S., and Palmer, M. (1999). Oligomerization of Vibrio cholerae cytolysin yields a pentameric pore and has a dual specificity for cholesterol and sphingolipids in the target membrane. J. Biol. Chem. *274*, 1375–1380. https://doi.org/10.1074/jbc.274.3.1375.

42. Zitzer, A., Wassenaar, T.M., Walev, I., and Bhakdi, S. (1997). Potent membrane-permeabilizing and cytocidal action of Vibrio cholerae cytolysin on human intestinal cells. Infect. Immun. *65*, 1293–1298. https://doi.org/10.1128/iai.65.4.1293-1298.1997.

43. Ikigai, H., Akatsuka, A., Tsujiyama, H., Nakae, T., and Shimamura, T. (1996). Mechanism of membrane damage by El Tor hemolysin of Vibrio cholerae O1. Infect. Immun. *64*, 2968–2973. https://doi.org/10.1128/iai.64.8.2968-2973.1996.

44. Olson, R., and Gouaux, E. (2005). Crystal structure of the Vibrio cholerae cytolysin (VCC) pro-toxin and its assembly into a heptameric transmembrane pore. J. Mol. Biol. *350*, 997–1016. https://doi.org/10.1016/j.jmb.2005.05.045.

45. Millet, Y.A., Alvarez, D., Ringgaard, S., von Andrian, U.H., Davis, B.M., and Waldor, M.K. (2014). Insights into Vibrio cholerae Intestinal Colonization from Monitoring Fluorescently Labeled Bacteria. PLoS Pathog. *10*, e1004405. https://doi.org/10.1371/journal.ppat.1004405.

46. Amin, A., Ali, A., Kurunathan, S., Cheong, T.G., Al-Jashamy, K.A., Jaafar, H., Zainuddin, Z.F., Ravichandran, M., and Lalitha, P. (2009). Comparison of histopathological features of Vibrio cholerae O1 El Tor and O139 Bengal infections in rabbit intestinal mucosa. Histol. Histopathol. *24*, 559–565. https://doi.org/10.14670/HH-24.559.

47. Fu, Y., Ho, B.T., and Mekalanos, J.J. (2018). Tracking Vibrio cholerae Cell-Cell Interactions during Infection Reveals Bacterial Population Dynamics within Intestinal Microenvironments. Cell Host Microbe *23*, 274–281.e2. https://doi.org/10.1016/j.chom.2017.12.006.

48. Krebs, S.J., and Taylor, R.K. (2011). Protection and attachment of Vibrio cholerae mediated by the toxin-coregulated pilus in the infant mouse model. J. Bacteriol. *193*, 5260–5270. https://doi.org/10.1128/JB.00378-11.

49. Adams, D.W., Stutzmann, S., Stoudmann, C., and Blokesch, M. (2019). DNA-uptake pili of Vibrio cholerae are required for chitin colonization and capable of kin recognition via sequence-specific self-interaction. Nat. Microbiol. *4*, 1545–1557. https://doi.org/10.1038/s41564-019-0479-5.

50. Kirn, T.J., Lafferty, M.J., Sandoe, C.M., and Taylor, R.K. (2000). Delineation of pilin domains required for bacterial association into microcolonies and intestinal colonization by Vibrio cholerae. Mol. Microbiol. *35*, 896–910. https://doi.org/10.1046/j.1365-2958.2000.01764.x.

51. Chiavelli, D.A., Marsh, J.W., and Taylor, R.K. (2001). The Mannose-Sensitive Hemagglutinin of Vibrio cholerae Promotes Adherence to Zooplankton. Appl. Environ. Microbiol. *67*, 3220–3225. https://doi.org/10.1128/AEM.67.7.3220-3225.2001.

52. Watnick, P.I., Fullner, K.J., and Kolter, R. (1999). A role for the mannose-sensitive hemagglutinin in biofilm formation by Vibrio cholerae El Tor. J. Bacteriol. *181*, 3606–3609. https://doi.org/10.1128/jb.181.11.3606-3609.1999.

53. Thelin, K.H., and Taylor, R.K. (1996). Toxin-coregulated pilus, but not mannose-sensitive hemagglutinin, is required for colonization by Vibrio cholerae O1 El Tor biotype and O139 strains. Infect. Immun. *64*, 2853–2856. https://doi.org/10.1128/iai.64.7.2853-2856.1996.

54. Kirn, T.J., and Taylor, R.K. (2005). TcpF is a soluble colonization factor and protective antigen secreted by E1 Tor and classical O1 and O139 Vibrio cholerae serogroups. Infect. Immun. *73*, 4461–4470. https://doi.org/10.1128/IAI.73.8.4461-4470.2005.

55. Kirn, T.J., Jude, B.A., and Taylor, R.K. (2005). A colonization factor links Vibrio cholerae environmental survival and human infection. Nature *438*, 863–866. https://doi.org/10.1038/nature04249.

56. Krachler, A.M., Ham, H., and Orth, K. (2011). Outer membrane adhesion factor multivalent adhesion molecule 7 initiates host cell binding during infection by gram-negative pathogens. Proc. Natl. Acad. Sci. USA *108*, 11614–11619. https://doi.org/10.1073/pnas.1102360108.

57. Syed, K.A., Beyhan, S., Correa, N., Queen, J., Liu, J., Peng, F., Satchell, K.J.F., Yildiz, F., and Klose, K.E. (2009). The Vibrio cholerae flagellar regulatory hierarchy controls expression of virulence factors. J. Bacteriol. *191*, 6555–6570. https://doi.org/10.1128/JB.00949-09.

58. Sperandio, V., Girón, J.A., Silveira, W.D., and Kaper, J.B. (1995). The OmpU outer membrane protein, a potential adherence factor of Vibrio cholerae. Infect. Immun. *63*, 4433–4438. https://doi.org/10.1128/iai.63.11.4433-4438.1995.

59. Matz, C., Bergfeld, T., Rice, S.A., and Kjelleberg, S. (2004). Microcolonies, quorum sensing and cytotoxicity determine the survival of Pseudomonas aeruginosa biofilms exposed to protozoan grazing. Environ. Microbiol. *6*, 218–226. https://doi.org/10.1111/j.1462-2920.2004.00556.x.

60. Jensen, P.Ø., Bjarnsholt, T., Phipps, R., Rasmussen, T.B., Calum, H., Christoffersen, L., Moser, C., Williams, P., Pressler, T., Givskov, M., and Høiby, N. (2007). Rapid necrotic killing of polymorphonuclear leukocytes is caused by quorum-sensing-controlled production of rhamnolipid by Pseudomonas aeruginosa. Microbiology *153*, 1329–1338. https://doi.org/10.1099/mic.0.2006/003863-0.

61. van Gennip, M., Christensen, L.D., Alhede, M., Phipps, R., Jensen, P.Ø., Christophersen, L., Pamp, S.J., Moser, C., Mikkelsen, P.J., Koh, A.Y., et al. (2009). Inactivation of the rhlA gene in Pseudomonas aeruginosa

prevents rhamnolipid production, disabling the protection against polymorphonuclear leukocytes. APMIS *117*, 537–546. https://doi.org/10.1111/j.1600-0463.2009.02466.x.

62. Alhede, M., Bjarnsholt, T., Jensen, P.Ø., Phipps, R.K., Moser, C., Christophersen, L., Christensen, L.D., van Gennip, M., Parsek, M., Høiby, N., et al. (2009). Pseudomonas aeruginosa recognizes and responds aggressively to the presence of polymorphonuclear leukocytes. Microbiology *155*, 3500–3508. https://doi.org/10.1099/mic.0.031443-0.
63. Ramamurthy, T., Nandy, R.K., Mukhopadhyay, A.K., Dutta, S., Mutreja, A., Okamoto, K., Miyoshi, S.I., Nair, G.B., and Ghosh, A. (2020). Virulence Regulation and Innate Host Response in the Pathogenicity of Vibrio cholerae. Front. Cell. Infect. Microbiol. *10*, 572096–572122. https://doi.org/10.3389/fcimb.2020.572096.
64. Qadri, F., Jonson, G., Begum, Y.A., Wennerås, C., Albert, M.J., Salam, M.A., and Svennerholm, A.M. (1997). Immune response to the mannose-sensitive hemagglutinin in patients with cholera due to Vibrio cholerae O1 and O139. Clin. Diagn. Lab. Immunol. *4*, 429–434. https://doi.org/10.1128/cdli.4.4.429-434.1997.
65. Hsiao, A., Liu, Z., Joelsson, A., and Zhu, J. (2006). Vibrio cholerae virulence regulator-coordinated evasion of host immunity. Proc. Natl. Acad. Sci. USA *103*, 14542–14547. https://doi.org/10.1073/pnas.0604650103.
66. Hsiao, A., Toscano, K., and Zhu, J. (2008). Post-transcriptional cross-talk between pro- and anti-colonization pili biosynthesis systems in Vibrio cholerae. Mol. Microbiol. *67*, 849–860. https://doi.org/10.1111/j.1365-2958.2007.06091.x.
67. Fu, Y., Waldor, M.K., and Mekalanos, J.J. (2013). Tn-seq analysis of vibrio cholerae intestinal colonization reveals a role for T6SS-mediated antibacterial activity in the host. Cell Host Microbe *14*, 652–663. https://doi.org/10.1016/j.chom.2013.11.001.
68. Olivier, V., Queen, J., and Satchell, K.J.F. (2009). Successful small intestine colonization of adult mice by Vibrio cholerae requires ketamine anesthesia and accessory toxins. PLoS One *4*, e7352. https://doi.org/10.1371/journal.pone.0007352.
69. Abel, S., and Waldor, M.K. (2015). Infant rabbit model for diarrheal diseases. Curr. Protoc. Microbiol. *38*, 6A.6.1–6A.6.15. https://doi.org/10.1002/9780471729259.mc06a06s38.
70. Schulte, L.N., Schweinlin, M., Westermann, A.J., Janga, H., Santos, S.C., Appenzeller, S., Walles, H., Vogel, J., and Metzger, M. (2020). An advanced human intestinal coculture model reveals compartmentalized host and pathogen strategies during Salmonella infection. mBio *11*, 033488-19. https://doi.org/10.1128/mBio.03348-19.
71. Floyd, K.A., Lee, C.K., Xian, W., Nametalla, M., Valentine, A., Crair, B., Zhu, S., Hughes, H.Q., Chlebek, J.L., Wu, D.C., et al. (2020). c-di-GMP modulates type IV MSHA pilus retraction and surface attachment in Vibrio cholerae. Nat. Commun. *11*, 1549. https://doi.org/10.1038/s41467-020-15331-8.
72. Sun, D., Lafferty, M.J., Peek, J.A., and Taylor, R.K. (1997). Domains within the Vibrio cholerae toxin coregulated pilin subunit that mediate bacterial colonization. Gene *192*, 79–85. https://doi.org/10.1016/S0378-1119(97)00007-3.
73. Edelstein, A.D., Tsuchida, M.A., Amodaj, N., Pinkard, H., Vale, R.D., and Stuurman, N. (2014). Advanced methods of microscope control using μManager software. J. Biol. Methods *1*, 10. https://doi.org/10.14440/jbm.2014.36.
74. Dobin, A., Davis, C.A., Schlesinger, F., Drenkow, J., Zaleski, C., Jha, S., Batut, P., Chaisson, M., and Gingeras, T.R. (2013). STAR: ultrafast universal RNA-seq aligner. Bioinformatics *29*, 15–21. https://doi.org/10.1093/bioinformatics/bts635.
75. Choi, M., Chang, C.-Y., Clough, T., Broudy, D., Killeen, T., MacLean, B., and Vitek, O. (2014). MSstats: an R package for statistical analysis of quantitative mass spectrometry-based proteomic experiments. Bioinformatics *30*, 2524–2526. https://doi.org/10.1093/bioinformatics/btu305.
76. Perez-Riverol, Y., Bai, J., Bandla, C., García-Seisdedos, D., Hewapathirana, S., Kamatchinathan, S., Kundu, D.J., Prakash, A., Frericks-Zipper, A., Eisenacher, M., et al. (2022). The PRIDE database resources in 2022: a hub for mass spectrometry-based proteomics evidences. Nucleic Acids Res. *50*, D543–D552. https://doi.org/10.1093/nar/gkab1038.
77. Oh, H., Siano, B., and Diamond, S. (2008). Neutrophil isolation protocol. J. Vis. Exp., 745. https://doi.org/10.3791/745.
78. Pleguezuelos-Manzano, C., Puschhof, J., van den Brink, S., Geurts, V., Beumer, J., and Clevers, H. (2020). Establishment and Culture of Human Intestinal Organoids Derived from Adult Stem Cells. Curr. Protoc. Immunol. *130*, e106. https://doi.org/10.1002/cpim.106.
79. Staab, J.F., Lemme-Dumit, J.M., Latanich, R., Pasetti, M.F., and Zachos, N.C. (2020). Co-Culture System of Human Enteroids/Colonoids with Innate Immune Cells. Curr. Protoc. Immunol. *131*, e113. https://doi.org/10.1002/cpim.113.
80. Gibson, D.G., Young, L., Chuang, R.Y., Venter, J.C., Hutchison, C.A., and Smith, H.O. (2009). Enzymatic assembly of DNA molecules up to several hundred kilobases. Nat. Methods *6*, 343–345. https://doi.org/10.1038/nmeth.1318.
81. Skorupski, K., and Taylor, R.K. (1996). Positive selection vectors for allelic exchange. Gene *169*, 47–52. https://doi.org/10.1016/0378-1119(95)00793-8.
82. Pédelacq, J.D., Cabantous, S., Tran, T., Terwilliger, T.C., and Waldo, G.S. (2006). Engineering and characterization of a superfolder green fluorescent protein. Nat. Biotechnol. *24*, 79–88. https://doi.org/10.1038/nbt1172.
83. Jaitin, D.A., Kenigsberg, E., Keren-Shaul, H., Elefant, N., Paul, F., Zaretsky, I., Mildner, A., Cohen, N., Jung, S., Tanay, A., and Amit, I. (2014). Massively parallel single-cell RNA-seq for marker-free decomposition of tissues into cell types. Science *343*, 776–779. https://doi.org/10.1126/science.1247651.
84. Brunelle, J.L., and Green, R. (2014). One-dimensional SDS-Polyacrylamide Gel Electrophoresis (1D SDS-PAGE). Methods Enzymol. *541*, 151–159. https://doi.org/10.1016/B978-0-12-420119-4.00012-4.
85. Wiśniewski, J.R., and Gaugaz, F.Z. (2015). Fast and sensitive total protein and Peptide assays for proteomic analysis. Anal. Chem. *87*, 4110–4116. https://doi.org/10.1021/ac504689z.
86. Ahrné, E., Glatter, T., Viganò, C., Schubert, C.v., Nigg, E.A., and Schmidt, A. (2016). Evaluation and Improvement of Quantification Accuracy in Isobaric Mass Tag-Based Protein Quantification Experiments. J. Proteome Res. *15*, 2537–2547. https://doi.org/10.1021/acs.jproteome.6b00066.
87. Huang, D.W., Sherman, B.T., and Lempicki, R.A. (2009). Systematic and integrative analysis of large gene lists using DAVID bioinformatics resources. Nat. Protoc. *4*, 44–57. https://doi.org/10.1038/nprot.2008.211.
88. Sherman, B.T., Hao, M., Qiu, J., Jiao, X., Baseler, M.W., Lane, H.C., Imamichi, T., and Chang, W. (2022). DAVID: a web server for functional enrichment analysis and functional annotation of gene lists (2021 update). Nucleic Acids Res. *50*, W216–W221. https://doi.org/10.1093/nar/gkac194.
89. Kong, A.T., Leprevost, F. v, Avtonomov, D.M., Mellacheruvu, D., and Nesvizhskii, A.I. (2017). MSFragger: ultrafast and comprehensive peptide identification in mass spectrometry–based proteomics. Nat. Methods *14*, 513–520. https://doi.org/10.1038/nmeth.4256.
90. Hartmann, R., Jeckel, H., Jelli, E., Singh, P.K., Vaidya, S., Bayer, M., Rode, D.K.H., Vidakovic, L., Díaz-Pascual, F., Fong, J.C.N., et al. (2021). Quantitative image analysis of microbial communities with BiofilmQ. Nat. Microbiol. *6*, 151–156. https://doi.org/10.1038/s41564-020-00817-4.
91. Jeckel, H., and Drescher, K. (2020). Advances and opportunities in image analysis of bacterial cells and communities. FEMS Microbiol. Rev. *45*, 1–14. https://doi.org/10.1093/femsre/fuaa062.
92. Otsu, N. (1979). A Threshold Selection Method from Gray-Level Histograms. IEEE Trans. Syst. Man Cybern. *9*, 62–66. https://doi.org/10.1109/tsmc.1979.4310076.

STAR★METHODS

KEY RESOURCES TABLE

REAGENT or RESOURCE	SOURCE	IDENTIFIER
Antibodies		
Goat anti-Rabbit IgG, Alexa Fluor 647	ThermoFisher	Cat#A-21244; RRID: AB_2535812
Goat anti-Mouse IgG, Alexa Fluor 647	ThermoFisher	Cat#A-21235; RRID: AB_2535804
Penta His Alexa Fluor Conjugate	Qiagen	Cat#35370
HA Tag Monoclonal antibody, Alexa Fluor 647	ThermoFisher	Cat#26183-A647; RRID: AB_2610626
Cholera Hemolysin Monoclonal Antibody	ThermoFisher	Cat#MA1-83520; RRID: AB_936752
Rabbit anti-MshA	Floyd et al.[71]	N/A
Rabbit anti-TcpA	Sun et al.[72]	N/A
Bacterial and virus strains		
Table S4	This paper	N/A
Chemicals, peptides, and recombinant proteins		
LB medium (Luria/Miller)	Carl Roth	Cat# X968.3
LB agar (Luria/Miller)	Carl Roth	Cat# X969.3
Gentamicin sulfate	Carl Roth	Cat#0233.4
Gentamicin sulfate	ITW Reagents	Cat#A1492
Kanamycin sulfate	Carl Roth	Cat#T832.3
Polymyxin B sulfate	AppliChem	Cat#A0890,0001
Streptomycin sulfate	Carl Roth	Cat#HP66.3
Gibco DMEM	ThermoFisher	Cat#11880028
GlutaMAX Supplement	ThermoFisher	Cat#35050038
Gibco Fetal bovine serum	ThermoFisher	Cat#10500064
X-Gal	Carl Roth	Cat#2315.3
IPTG	Goldbio	Cat#I2481C5
L(+)-Arabinose	Carl Roth	Cat#5118.2
Dimethyl sulfoxide (DMSO)	Carl Roth	Cat#7820.4
Lymphoprep	STEMCELL Technologies	Cat#07801
CD14 Micro-Beads human	Milteny Biotec	Cat#130-050-201
CD4 Micro-Beads human	Milteny Biotec	Cat#130-045-101
CD19 Micro-Beads human	Milteny Biotec	Cat#130-050-301
CD56 Micro-Beads human	Milteny Biotec	Cat#130-050-401
TheraPEAK X-VIVO™-15 Serum-free Hematopoietic Cell Medium	Lonza	Cat#BEBP02-061Q
Recombinant Human GM-CSF	Peprotech	Cat#300-03
Phorbol 12-myristate 13-acetate (PMA)	Sigma-Aldrich	Cat#P1585-1MG
Corning Matrigel	Corning	Cat#356231
Gibco Advanced DMEM/F-12	ThermoFisher	Cat#12634010
Gibco HEPES	ThermoFisher	Cat#15630106
Gibco B-27 Supplement	ThermoFisher	Cat#12587010
Gibco N-2 Supplement	ThermoFisher	Cat#17502001
N-acetyl-L-cysteine	Sigma-Aldrich	Cat#A9165
Nicotinamide	Sigma-Aldrich	Cat#N0636
Human EGF	Sigmal-Aldrich	Cat#E9644
Recombinant Human RSPO1-Fc	SUN Bioscience, EPFL	N/A

(*Continued on next page*)

Continued

REAGENT or RESOURCE	SOURCE	IDENTIFIER
Recombinant Human Noggin-Fc	SUN Bioscience, EPFL	N/A
SB202190	Sigma-Aldrich	Cat#S7067
A 83-01	Sigma-Aldrich	Cat#SML0788
Prostaglandin E2	Lucerna-Chem	Cat#HY-101952
Human [Leu15]-gastrin I	Sigma-Aldrich	Cat#G9145
Wnt-surrogate-Fc Fusion Recombinant Protein	ThermoFisher	Cat#PHG0401
Amphotericin B	ThermoFisher	Cat#15290018
Thiazovivin	Sigma-Aldrich	Cat#SML1045
CHIR99021	Sigma-Aldrich	Cat#361571
TrypLE Express Enzyme	ThermoFisher	Cat#12605010
SmBM Basal Medium	Lonza	Cat#CC-3181
SingleQuots supplements	Lonza	Cat#CC-4149
Rat-tail collagen type I	Sigma-Aldrich	Cat#C3867
CellTracker Deep Red Dye	ThermoFisher	Cat#C34565
CellTracker Red CMTPX Dye	ThermoFisher	Cat#C34552
Gibco HBSS	ThermoFisher	Cat#14175053
Propidium iodide	Carl Roth	Cat#CN74.3
CellMask Plasma Membrane Stain	ThermoFisher	Cat#10046
Sylgard 184 Silicone Elastomer Kit	DOW	Cat# 1673921
Formaldehyde	Sigma-Aldrich	Cat#F8775-25ML
Bovine serum albumin	Sigma-Aldrich	Cat#A3059-100G
RNAlater	Qiagen	Cat#76106
TURBO DNase	ThermoFisher	Cat#AM2238
Trichloroacetic acid	Sigma-Aldrich	Cat#T6399
Critical commercial assays		
IL-1 beta human uncoated ELISA Kit	ThermoFisher	Cat#88-7261-22
IL-8 human uncoated ELISA Kit	ThermoFisher	Cat#88-8086-22
TNF alpha human uncoated ELISA Kit	ThermoFisher	Cat#88-7346-22
mirVana miRNA Isolation Kit	ThermoFisher	Cat#AM1560
Deposited data		
Raw and analyzed transcriptome data	Gene Expression Omnibus	GEO: GSE184077, GSE184078
Mass spectrometry data	ProteomeXchange Consortium	PRIDE: PXD039577, PXD039579
Experimental models: Cell lines		
THP-1	ATCC	ATCC TIB-202
Human intestinal epithelial cells	Lonza	Cat#CC-2931; Lot 0000751359
Human intestinal myofibroblasts	Lonza	Cat#CC-2902; Lot 0000662132
3dGRO Duodenum Intestinal Organoids	Merck	Cat#SCC324
Oligonucleotides		
Table S6	This paper	N/A
Recombinant DNA		
Table S5	This paper	N/A
Software and algorithms		
Custom image analysis code	This paper	https://doi.org/10.5281/zenodo.7900472
Nikon NIS-Elements AR	Nikon	Version 4.51.01
MATLAB	MathWorks	Version R2017b
Prism	GraphPad Software	Version 9.3.1

(*Continued on next page*)

Continued

REAGENT or RESOURCE	SOURCE	IDENTIFIER
Micro-Manager	Edelstein et al.[73]	Version 2.0
STAR	Dobin et al.[74]	Version 2.5.3a
Spectronaut	Biognosys	Version 15.7.220308.50606
MSstats	Choi et al.[75]	Version 4.2.0

RESOURCE AVAILABILITY

Lead contact

Requests for further information, resources or reagents should be addressed to the lead contact, Knut Drescher (knut.drescher@unibas.ch).

Materials availability

Requests for strains, cell lines, and plasmids should be addressed to the lead contact.

Data and code availability

- Raw and analyzed transcriptome data are available at the United States National Center for Biotechnology Information Gene Expression Omnibus. The mass spectrometry proteomics data have been deposited to the ProteomeXchange Consortium via the PRIDE[76] partner repository. Accession numbers are listed in the key resources table. Microscopy data will be shared by the lead contact upon request.
- The original code that was used for image analysis is publicly available on Zenodo at the DOI listed in the key resources table.
- Any additional information required to reanalyze the data reported in this paper is available from the lead contact upon request.

EXPERIMENTAL MODEL AND SUBJECT DETAILS

Bacterial growth conditions

All *V. cholerae* strains used in this study are derivatives of the wild type *V. cholerae* O1 biovar El Tor strain C6706 (KDV201). Routinely, bacteria were grown in LB medium (Luria/Miller) supplemented with the appropriate antibiotics at 37°C and 250 rpm shaking.

For experiments probing the interaction of *V. cholerae* with immune cells, bacteria were first grown in LB medium supplemented with gentamicin (final concentration 30 μg mL^{-1}) until exponential growth phase. Afterward, cells were back-diluted 1:500 and re-grown in Dulbecco's Modified Eagle's Medium (DMEM; Gibco cat. no. 11880028) with GlutaMax (Gibco cat. no. 35050038) supplemented with 10% (v/v) fetal calf serum (FCS; Gibco cat. no. 10500064) and gentamicin until stationary growth phase.

Cell culture and differentiation of immune cells

Leukocytes were isolated from blood buffy coats, which were obtained from healthy donors (deidentified prior to use) from the Center for Transfusion Medicine and Haemotherapy in Giessen, Germany. All donors consented the use of their blood samples for scientific research. The leukocytes were then isolated using the Lymphoprep density gradient medium (STEMCELL Technologies cat. no. 07801) and were further separated into monocytes, CD4$^+$ T cells, B cells, as well as NK cells with the help of Milteny MACS MicroBeads (CD14, CD4, CD19, CD56) according to the manufacturer's protocol. Isolated monocytes, CD4$^+$ T cells, B cells, and NK cells were immediately used for interaction studies of *V. cholerae* and the immune cells, as described in the section on *V. cholerae*-immune cells interaction studies.

To obtain macrophages, 8×10^4 of the freshly isolated monocytes (isolated as described in the previous paragraph) were suspended in 200 μL X-Vivo 15 medium (Lonza cat. no. BEBP02-061Q) supplemented with 5% (v/v) FCS. Afterward, the cells were seeded in an individual well of a 96-well glass bottom plate (Greiner Bio-One cat. no. 655892) and treated with 15 ng mL^{-1} human recombinant GM-CSF (Preprotech cat. no. 300-03) for 7 days at 37°C in a humidified 5% CO_2 incubator before interaction studies with *V. cholerae* were conducted (described in the next section). After 4 days of differentiation, a further 50 μL of fresh medium together with 15 ng mL^{-1} human recombinant GM-CSF were added to the well. In case macrophages were used for interaction studies that included enteroid monolayers, 8×10^4 of the freshly isolated monocytes were suspended in 50 μL of medium containing 15 ng mL^{-1} human recombinant GM-CSF and seeded in the center of an individual well of a 12-well glass bottom plate (Cellvis cat. no. P12-1.5H-N). The following day, additional 950 μL medium were added. After 4 days of differentiation, a further 200 μL of fresh medium together with 15 ng mL^{-1} human recombinant GM-CSF were added to the well.

To obtain neutrophils, blood samples were taken from healthy human donors, who were fully informed and consented to providing samples for this study. Donated blood was handled in accordance with the ethics regulations of the Philipps-Universität Marburg

(permit: AZ 143/20). Neutrophils were isolated from whole blood according to the protocol published by Oh et al.[77] and used immediately for interaction studies with *V. cholerae* as described in the section on *V. cholerae*-immune cells interaction studies.

In addition to the primary cells described above, the human monocytic cell line THP-1 (ATCC TIB-202) was used in this study. THP-1 cells were grown in DMEM medium with GlutaMax, supplemented with 10% (v/v) FCS and gentamicin (final concentration 30 μg mL^{-1}) in T75 or T175 flasks in a humidified 37°C, 5% CO_2 incubator. To differentiate THP-1 monocytes into macrophages, 2.5×10^4 cells suspended in 200 μL of fresh medium were seeded in an individual well of a 96-well glass bottom plate and treated with 20 nM phorbol 12-myristate 13-acetate (PMA; Sigma cat. no. P1585-1MG) for 72 h at 37°C and 5% CO_2. For experiments which required cell differentiation in 12-well tissue culture plastic plates, 2.5×10^5 monocytes per well were used and each well was filled with 1 mL of medium. In case monocytes were differentiated in tissue culture dishes (60 mm in diameter), $1.5x10^6$ monocytes were seeded into 5 mL of medium. When macrophages were required for interaction studies including enteroid monolayers, 2.5×10^4 monocytes were suspended in 50 μL of medium containing PMA and seeded in the center of an individual well of a 12-well glass bottom plate. After one day, the total volume in each well was increased to 1 mL and monocytes were left to differentiate for two more days. After differentiation, macrophages were used for *V. cholerae* interaction studies as described in the methods section "*V. cholerae*-immune cell interaction studies".

Culturing human enteroids

Human intestinal epithelial cells (donor #1, Lonza cat. no. CC-2931, Lot 0000751359, primary cells isolated from fetal small intestine) were embedded in Matrigel (Corning cat. no. 356231) and grown into enteroids in a humidified incubator at 37°C and 5% CO_2, using human organoids expansion medium (hOEM). hOEM was composed of Basal medium (Advanced DMEM/F-12 [ThermoFisher cat. no. 12634010], 10 mM HEPES [ThermoFisher cat. no. 15630106], 1% GlutaMAX [ThermoFisher cat. no. 35050061]) supplemented with 2% B-27 Supplement (ThermoFisher cat. no. 12587010), 1% N-2 Supplement (ThermoFisher cat. no. 17502001), 1 mM N-acetyl-L-cysteine (Sigma-Aldrich cat. no. A9165), 10 mM nicotinamide (Sigma-Aldrich cat. no. N0636), 50 ng mL^{-1} Human EGF (Sigma-Aldrich, E9644), 500 ng mL^{-1} recombinant Human RSPO1-Fc (SUN Bioscience, EPFL), 100 ng mL^{-1} recombinant Human Noggin-Fc (SUN Bioscience, EPFL), 10 μM SB202190 (Sigma-Aldrich cat. no. S7067), 500 nM A 83-01 (Sigma-Aldrich cat. no. SML0788), 10 nM Prostaglandin E2 (Lucerna-Chem cat. no. HY-101952), 10 nM human [Leu15]-gastrin I (Sigma-Aldrich cat. no. G9145), 0.5 nM Wnt-surrogate-Fc (ThermoFisher cat. no. PHG0401), 30 μg mL^{-1} gentamicin (ITW Reagents cat. no. A1492) and 0.25 μg mL^{-1} amphotericin B (ThermoFisher cat. no. 15290018). Grown enteroids were passaged as described previously.[78,79] Briefly, Matrigel domes were dissolved in ice-cold Basal medium, collected and pelleted for 5 min (200 g, 4°C). The enteroid pellet was resuspended by active pipetting in 1 mL of ice-cold Basal medium before additional 9 mL of ice-cold Basal medium were added. After a second centrifugation step, enteroids were resuspended in freshly thawed Matrigel. A droplet containing 25 μL of the enteroid suspension was added to a well of a 24-well plate (Corning cat. no. 3526) and the Matrigel domes were polymerized for 15 min at 37°C before 500 μL hOEM supplemented with 2 μM thiazovivin (Sigma-Aldrich cat. no. SML1045) and 2.5 μM CHIR99021 (Sigma-Aldrich cat. no. 361571) were added. Enteroids were passaged every 4–5 days at a ratio of 1:2 or 1:3 depending on the density. Enteroids were used for experiments between passages 3 and 10.

For experiments shown in Figure S6 we used organoids from donor #2 (3dGRO Duodenum Intestinal Organoids, Merck/Sigma-Aldrich cat. no. SCC324, isolated from a 33-year old female donor). These donor #2 enteroids were cultured according to the manufacturer's protocol and passaged as described above.

Culturing differentiated human enteroid monolayers

Enteroid monolayers from donor #1 were generated according to the manufacturer's protocols. Briefly, enteroids were collected by centrifugation (5 min, 200 g, 4°C) and broken down to single cells using 1 mL TrypLE (ThermoFisher cat. no. 12605010). Single cells were passed through a 40 μm cell strainer (pluriSelect cat. no. PS-43-10040-40), centrifuged (5 min, 200 g, 4°C) and resuspended in SmBM-2 (Lonza cat. no. CC-3181), supplemented with SingleQuote Supplements (Lonza cat. no. CC-4149). The cell number was adjusted to $1.15x10^6$ cells mL^{-1} and 100 μL of the cell suspension was added onto a 3 μm transparent PET membrane insert (Falcon cat. no. 353096) which was pre-coated with rat-tail collagen type I (30 μg mL^{-1}; Sigma-Aldrich cat. no. C3867). Inserts were placed on top of human myofibroblasts (Lonza cat. no. CC-2902, Lot 0000662132). Human myofibroblasts were cultured according to the manufacturer's protocol and $1x10^5$ cells were seeded the day before in a well of a 24-well cell culture plate (Corning cat. no. 3526) filled with 1 mL of SmBM-2 (Lonza cat. no. CC-3181), supplemented with SingleQuote Supplements (Lonza cat. no. CC-4149). To achieve cell differentiation and generation of an epithelial monolayer, human small intestinal epithelial cells were co-cultured with myofibroblasts for 6 days in a humidified incubator at 37°C and 5% CO_2. The medium was replaced the next day after seeding and then every other day. The confluent epithelial monolayer after 6 days of differentiation consisted of approximately $9.1x10^4$ cells (mean value on PET membrane from n = 4 independent seedings).

Donor #2 enteroid monolayers were generated from 3dGRO Duodenum Intestinal Organoids (Merck/Sigma-Aldrich cat. no. SCC324) using an analogous protocol to the one described for donor #1 in the paragraph above. The single cell suspension was created with a similar protocol as described for the Lonza organoids above. After passing the cells through a cell strainer and a final centrifugation step, the cells were resuspended in hOEM, supplemented with 2 μM thiazovivin (Sigma-Aldrich cat. no. SML1045) and 2.5 μM CHIR99021 (Sigma-Aldrich cat. no. 361571). The cell number was adjusted to $1x10^6$ cells mL^{-1} and 100 μL of the cell suspension was added onto a 3 μm transparent PET membrane insert (Falcon cat. no. 353096) which was pre-coated with rat-tail

collagen type I (30 μg mL^{-1}; Sigma-Aldrich cat. no. C3867). The insert was placed into a well of a 24-well cell culture plate (Corning cat. no. 3526) filled with 500 μL of hOEM, supplemented with 2 μM thiazovivin (Sigma-Aldrich cat. no. SML1045) and 2.5 μM CHIR99021 (Sigma-Aldrich cat. no. 361571). The cells were incubated for 7 days in a humidified incubator at 37°C and 5% CO_2 in order to form a uniform monolayer. The medium was exchanged one day after seeding the cells onto the membrane and then every other day until day 7 using fresh hOEM, supplemented with 2 μM thiazovivin (Sigma-Aldrich cat. no. SML1045) only. From day 7, the cells were cultured in human organoids differentiation medium hODM (Basal medium supplemented with 2% B-27TM supplement [ThermoFisher cat. no. 12587010], 1% N-2 supplement [ThermoFisher cat. no. 17502001], 1 mM N-acetyl-L-cysteine [Sigma-Aldrich cat. no. A9165], 50 ng mL-1 Human EGF, 100 ng mL-1 recombinant Human Noggin-Fc, 500 nM A-83-01, 10 nM human [Leu15]-gastrin I [Sigma-Aldrich cat. no. G9145], 30 μg mL-1 gentamicin [ITW Reagents cat. no. A1492]) for five more days until the monolayers were fully differentiated.[79] The confluent epithelial monolayer after 12 days of differentiation consisted of approximately $31x10^4$ cells (mean value on PET membrane from n = 3 independent seedings). The data corresponding to this protocol is shown in Figure S6.

METHOD DETAILS

Bacterial strain construction

Bacterial strains, plasmids and oligonucleotides used in this study are listed in Tables S4, S5, and S6. To generate gene deletions, 1 kbp flanking regions of the gene of interest from *V. cholerae* as well as the plasmid pNUT144 were amplified and the polymerase chain reaction (PCR) products were assembled via Gibson assembly.[80] The resulting plasmid was conjugated into strain KDV201 and bacteria were selected according to a previously described protocol.[81] After the final selection step, bacteria were screened for the gene deletion by PCR.

V. cholerae expressing TcpF with a C-terminal 6x Histidine (His)-Tag was generated by exchanging wild type *tcpF* with a Histidine (His)-tagged *tcpF.* For this, plasmid pNUT2130 was constructed and conjugated into *V. cholerae* and successful gene replacement was confirmed by PCR and DNA sequencing. Similarly, *V. cholerae* strains expressing RbmA and RbmC with a C-terminal 6x Histidine (His)-Tag or Bap1 with a C-terminal Hemagglutinin (HA)-Tag were generated and the plasmids pNUT918, pNUT2061 and pNUT2049 were used for conjugation respectively.

Complementation strains were obtained by inserting the gene of interest (*mshA*, *flaA*) together with its native promoter into the *lacZ* site of *V. cholerae.* For this, the gene of interest, its promoter and the plasmid pNUT276 were amplified and the PCR products were assembled into a plasmid via Gibson assembly.[80] The plasmid was then conjugated into *V. cholerae* and cells were selected as described above. DNA insertion into the *lacZ* site was confirmed with blue/white screening of bacterial colonies using 5-bromo-4-chloro-3-indolyl-β-D-galactopyranoside (X-Gal, final concentration 40 μg mL^{-1}).

To generate a fluorescent transcriptional reporter for investigating *vps* expression, *sfgfp* was inserted into the native *vps* locus between *vpsF* and *vpsG* using the plasmid pNUT2111.

For overexpression of ToxT in *V. cholerae*, the arabinose inducible promoter P_{BAD} and *toxT* were integrated together into the *lacZ* site on the chromosome. To accomplish this, a plasmid based on pNUT276 was constructed, harboring *toxT* and P_{BAD}. This plasmid was conjugated into *V. cholerae* and bacteria were selected for insertion of the DNA fragment.

Overexpression of the hemolysin HlyA in *V. cholerae* was achieved using the overexpression plasmid pNUT2425. For construction of this plasmid, *V. cholerae hlyA* and the backbone of plasmid pNUT1246 were amplified and joined via Gibson assembly.[80] The resulting plasmid was then conjugated into *V. cholerae* to generate the overexpression strain.

To overexpress RocS and CdgJ in *V. cholerae*, the overexpression plasmid pNUT3068 was constructed. For this, *V. cholerae rocS* and *cdgJ* as well as the backbone of plasmid pNUT1246 were amplified and joined via Gibson assembly.[80] The resulting plasmid was then conjugated into *V. cholerae* to generate the overexpression strain.

In general, plasmid clones based on the pKAS32-derived suicide vector pNUT144 were first constructed in the *Escherichia coli* strain S17-1 λ*pir*. Afterward, the plasmids were conjugated into *V. cholerae.* Plasmids with a pSC101 origin of replication were constructed in *E. coli* strain Top10 and then transferred to *V. cholerae* with the help of an additional *E. coli* strain harboring the conjugation helper plasmid pRK600 via triparental mating.

To enable constitutive production of sfGFP for fluorescence imaging of *V. cholerae* cells, the plasmid pNUT542 containing the superfolder green fluorescent protein gene (*sfgfp*)[82] under control of the promoter P_{tac} was conjugated into all final strains of *V. cholerae* except for hemolysin overexpression strains. For these strains, P_{tac}-*sfgfp* was integrated with the help of plasmid pNUT480 into the *lacZ* site on the chromosome of *V. cholerae*.

V. cholerae-immune cell interaction studies

For interaction studies with freshly isolated monocytes, neutrophils, $CD4^+$ T cells, B cells, and NK cells, the immune cells were stained with CellTracker Deep Red Dye (ThermoFisher cat. no. C34565; final concentration 0.75 μM; suspended in Hanks Balanced Salt Solution (HBSS)) or CellTracker Red CMTPX Dye (ThermoFisher cat. no. C34552; final concentration 3 μM; suspended in HBSS) for 15 min at 37°C in a humidified 5% CO_2 incubator. Stained immune cells were pelleted (200 g, 5 min) to remove the staining solution and resuspended in DMEM with GlutaMax, supplemented with 10% (v/v) FCS and gentamicin (final concentration 30 μg mL^{-1}). The cell number was adjusted to 4.572×10^5 cells mL^{-1} and 175 μL of the cell suspension (corresponding to 8×10^4 immune cells) were added to a well of a 96-well glass-bottom plate. Immediately afterward, the immune cells were exposed to *V. cholerae*. For this,

grown bacteria (bacterial growth conditions were as described above) were washed once and diluted to 4.1×10^8 cells mL^{-1} using fresh cell culture medium. Subsequently, 25 μL of the bacterial suspension were added to the immune cells, resulting in an MOI of 128 at the time of seeding, and the cell-cell interaction was monitored by fluorescence confocal microscopy. In total, the well was filled with 200 μL of liquid.

For experiments with macrophages, the entire differentiation medium was removed after 3 days (THP-1 cell line) or 7 days (primary cells) from the wells of the 96-well glass-bottom plate, and the glass surface attached macrophages were stained with 100 μL staining solution (CellTracker suspended in HBSS as described above) for 15 min at 37°C in a humidified 5% CO_2 incubator. Afterward, the staining solution was removed and macrophages were washed once with HBSS followed by exposure to *V. cholerae*. The bacterial suspension was prepared as described in the previous paragraph except that bacteria were diluted to 1.6×10^7 cells mL^{-1} when THP-1 monocyte derived macrophages were studied. When primary cells were used, the bacterial suspension was prepared to contain 5.12×10^7 cells mL^{-1}. If necessary, the cell culture medium was supplemented with propidium iodide (final concentration 8 μM) before the bacterial suspension was generated, which enabled the detection of dead macrophages during the *V. cholerae*-macrophage interaction study. Finally, 200 μL of the bacterial suspension were added to stained and washed macrophages and fluorescence confocal imaging was started immediately.

In case *V. cholerae*-macrophage interaction studies were performed in 12-well plastic bottom plates, THP-1 monocyte derived macrophages and bacteria were prepared as described in the previous paragraph except that 500 μL staining solution was used in order to fluorescently stain the macrophages. Furthermore, the bacterial suspension contained 1.73×10^7 cells mL^{-1} and 1 mL of this suspension was added to the stained and washed $1.35\text{x}10^5$ macrophages, resulting in an initial MOI of 128.

For *V. cholerae*-immune cell interaction experiments including enteroid monolayers, macrophages were prepared as described above except that 1 mL of staining solution was used. After staining, 500 μL of fresh SmBM-2 (supplemented with SingleQuots Supplements and 30 μg mL^{-1} gentamicin) or hODM (supplemented with 30 μg mL^{-1} gentamicin) were added to stained macrophages. The enteroid monolayers (prepared as described in the section "Culturing differentiated human enteroid monolayers") were stained with CellMask Deep Red Plasma membrane stain (ThermoFisher cat. no. C10046, final concentration 2.5 μg mL^{-1}, suspended in hODM or SmBM supplemented with SingleQuots Supplements) in a humidified incubator at 37°C, 5% and CO_2 for 30 min. Stained enteroid monolayers were washed once with fresh medium before 50 μL of SmBM-2 (supplemented with SingleQuots Supplements and 30 μg mL^{-1} gentamicin) or hODM (supplemented with 30 μg mL^{-1} gentamicin) were added to the apical side. Afterward, membrane inserts harboring intestinal epithelial monolayers were placed on top of macrophages and fixed in position using a poly(dimethylsiloxane) (PDMS) holder. Grown bacteria were washed once using Basal medium and diluted to $6.4\text{x}10^7$ cells mL^{-1} in fresh SmBM-2 medium (supplemented with SingleQuots Supplements and 30 μg mL^{-1} gentamicin) or hODM (supplemented with 30 μg mL^{-1} gentamicin). Subsequently, 50 μL of the bacterial suspension were added to the apical side of the differentiated enteroid monolayers and the interaction of *V. cholerae* with the epithelial cells and the macrophages was monitored using fluorescence confocal microscopy. For most experiments including intestinal epithelial monolayers, the 50 μL of bacterial seeding suspension contained $3.2\text{x}10^6$ *V cholerae* cells, except for experiments in which the MOI was varied (Figure S5B). Below the intestinal epithelial monolayers, we cultured $2.5\text{x}10^4$ macrophages for experiments based on THP-1 cells, or $8\text{x}10^4$ macrophages for experiments based on primary cells.

Immunofluorescence-based visualization of MSHA pili, TC pili, and the secreted proteins TcpF, RbmA, RbmC, Bap1, and HlyA

To visualize MSHA pili and TC pili in biofilms formed on the surface of macrophages (differentiated in 96-well glass-bottom plates), THP-1 monocyte-derived macrophages were exposed to *V. cholerae* for 4 h at 37°C and 5% CO_2. Afterward, the entire culture medium was removed from the well and the sample was fixed by adding 100 μL of a 4% paraformaldehyde solution (Sigma cat. no. F8775-25ML; diluted in 1x phosphate buffered saline, PBS, pH 7). This step, and all subsequent steps, were performed at room temperature. After an incubation time of 10 min, the fixation solution was removed and 200 μL of 2% bovine serum albumin (BSA; Sigma cat. no. A3059-100G; dissolved in 1x PBS, pH 7) was added to the well. Following incubation for 1 h, BSA was removed and 100 μL of primary antibodies against MshA or TcpA [rabbit anti-MshA,[71] or rabbit anti-TcpA[72]] was added to the well at a final concentration of 2 μg mL^{-1} (diluted in 1x PBS, pH 7). The antibody was removed after 2 h and the wells were washed three times using 200 μL of 1x PBS pH 7 with 10 min incubation between each washing step. Subsequently, 100 μL of the secondary anti-rabbit antibody conjugated to Alexa Fluor 647 (ThermoFisher cat. no. A-21244) was added at a final concentration of 2 μg mL^{-1} (diluted in 1x PBS, pH 7). After 2h, the wells were washed three times as described above and the samples were fixed a second time using 100 μL of a 4% paraformaldehyde solution for 10 min. Finally, the samples were stored in 100 μL of 1x PBS (pH 7) at 4°C until fluorescence imaging was performed.

In case MSHA pili and TC pili were visualized in biofilms on macrophages during co-culture experiments with human small intestinal epithelial monolayers, co-culture experiments were setup as described in the section "*V. cholerae*-immune cell interaction studies", and bacterial biofilm formation on macrophages was monitored by confocal fluorescence microscopy. At the time point when thick biofilms were observed on the surface of macrophages, the entire culture medium including the insert harboring the intestinal monolayer was removed. Then, the same protocol for fixation and antibody labeling as described above was applied, with only one modification: 500 μL of liquid was used for each step in order to cover the whole surface of the well.

The secreted proteins TcpF, RbmA, RbmC, Bap1 and HlyA were visualized via immunofluorescence staining of live samples. In the case of TcpF, RbmA and RbmC, macrophages were exposed to *V. cholerae* expressing the protein of interest harboring a C-terminal

6x Histidine (His)-Tag and the cell culture medium was supplemented with anti-6x-His-Tag antibodies conjugated to Alexa Fluor 647 (Qiagen cat. no. 35370; final concentration 0.4 μg mL^{-1}) during live-cell imaging. When Bap1 was investigated, macrophages were exposed to *V. cholerae* expressing Bap1 with a C-terminal Hemagglutinin (HA)-Tag and the medium was supplemented with anti-HA-Tag antibodies conjugated to Alexa Fluor 647 (ThermoFisher cat. no. 26183-A647) with a final concentration of 0.4 μg mL^{-1}. For the visualization of HlyA, macrophages were exposed to *V. cholerae* cells that were overexpressing *hlyA*. The cell culture medium was supplemented with 0.1 mM IPTG for the overproduction of HlyA, as well as 4 μg mL^{-1} mouse anti-HlyA antibody (ThermoFisher cat. no. MA1-83520) together with a secondary anti-mouse antibody conjugated to Alexa Fluor 647 (ThermoFisher cat. no. A21235; 4 μg mL^{-1} final concentration).

Measurements of bacterial growth in the presence of different macrophage lysate concentrations

To investigate the effect of lysed macrophages on the growth of *V. cholerae*, $3x10^6$ monocytes were differentiated into macrophages in tissue culture dishes as described above. Afterward, the differentiation medium was removed and macrophages were scraped off the surface using a cell scraper. Macrophages were collected and resuspended in 1 mL of fresh DMEM with GlutaMax, supplemented with 10% (v/v) FCS and gentamicin (final concentration 30 μg mL^{-1}). To generate macrophage lysate, immune cells were lysed by sonication for 10 min at 4°C (sonication settings: 3 s on, 90 s off, 50% amplitude, 50% constant) and the cell debris was removed by centrifugation for 1 min at 12.000 rpm. The macrophage lysate was used immediately for bacterial growth studies. *V. cholerae* cells were grown first in LB medium with gentamicin (final concentration 30 μg mL^{-1}) and then transferred to DMEM with GlutaMax, supplemented with 10% (v/v) FCS and gentamicin (final concentration 30 μg mL^{-1}) as described in the section ''Bacterial growth conditions'' above. Grown bacteria were washed once with fresh DMEM (supplemented with GlutaMax, 10% (v/v) FCS and gentamicin) and subsequently $3.2x10^6$ bacterial cells were added to each well of a 96-well plate. Each well contained 200 μL of liquid based on DMEM supplemented with GlutaMax, 10% (v/v) FCS and gentamicin, but also including different concentrations of macrophage lysate. Bacterial growth was monitored at 37°C in an automated plate reader.

Confocal fluorescence microscopy

To monitor the interaction between *V. cholerae* and human immune cells, fluorescence confocal images were taken with a Yokogawa CSU spinning disk unit mounted on a Nikon Ti-Eclipse inverted microscope using a 40x oil NA 1.3 objective (Nikon) and an Andor iXon-Ultra EMCCD camera. Experiments involving enteroid monolayers were imaged with a 20x air NA 0.75 objective. In addition, three lasers (488nm, 552 nm, 637 nm) were used for the excitation of fluorescent proteins and dyes. Images were acquired every 30 min at low excitation light intensities and 30 ms exposure time, using the EM-gain of the EMCCD camera. Focus drifts were corrected using the hardware autofocus system (PFS, Nikon). The hardware was controlled by Micro-Manager[73] or by NIS Elements (Nikon). Secreted proteins and type IV pili visualized by immunofluorescence staining were imaged with a 100x oil NA 1.45 objective (Nikon). For biofilm architecture analyses and tracking of bacterial growth on the macrophage surface a 100x oil NA 1.45 objective (Nikon) was used and an additional 2× lens was placed between the CSU and the Nikon Ti-E side port. The microscope was equipped with an incubation chamber to control the temperature and the CO_2 levels during live-cell imaging.

Enzyme-linked immunosorbent assay (ELISA)

Sandwich ELISA was used to quantify secreted cytokines during *V. cholerae*-macrophage interactions (IL-1β, IL-8, TNF-α). Culture supernatants were collected 4 h after start of co-incubation, which corresponds to approximately 20 min before bacterial biofilm dispersal was predicted to take place. At this interaction time point, only very few macrophages are dead (Figure S2C, blue line). The ELISA kits were purchased from ThermoFisher (cat. no. 88–7261, 88–8086, 88-7346-22) and the experiment was conducted according to the manufacturer's instructions.

Sample preparation for bacterial RNA-sequencing

For RNA-sequencing, *V. cholerae*-macrophage interaction assays were performed in 12-well plastic bottom plates. After exposure of THP-1 derived macrophages to *V. cholerae* for a defined time at 37°C in a humidified 5% CO_2 incubator, the samples were fixed with RNA*later* (Qiagen, cat. no. 76106). The culture supernatant was collected. Attached cells remaining in the well were scraped and collected separately. Following centrifugation at 4°C with 2000 g for 10 min, cell pellets were snap-frozen in liquid nitrogen and stored at −80°C until RNA extraction was performed using the mirVana Kit (Ambion, cat. no. AM1560) according to the manufacturer's instructions. The RNA quality was checked using electrophoresis (Agilent 2100 Bioanalyzer). Sequencing library preparation and the Illumina sequencing were carried out by Vertis Biotechnologie AG, Freising-Weihenstephan, Germany.

Bacterial read processing and mapping statistics after bacterial RNA sequencing

Fastq reads were aligned to a reference genome *V. cholerae* O1 biovar El Tor str. N16961 (NCBI reference sequence NC_002505.1 and NC_002506.1) using STAR[74] (version 2.5.3a). Read counts were calculated using STAR. Data were normalized to a library size factor. Factors were calculated by dividing the total number of reads from each sample to the median of the total number of reads across all samples. Data were transformed to a $\log_2$ scale. A minimal expression threshold was set to 5. Fold change was calculated for each sample from an average of all naive samples. Principal component analysis (PCA) was performed on all genes. A threshold of 1.5 was set to identify upregulated genes.

Sample preparation for macrophage RNA sequencing

For RNA-sequencing, *V. cholerae*-macrophage interaction assays were performed in 12-well plastic bottom plates. After exposure of THP-1 derived macrophages to *V. cholerae* for a defined time at 37°C in a humidified 5% CO_2 incubator, the samples were fixed with RNA*later* (Qiagen, cat. no. 76106). The culture supernatant was removed. Attached cells remaining in the well were scraped and collected. Following centrifugation at 4°C with 2000 g for 10 min, cell pellets were snap-frozen in liquid nitrogen and stored at −80°C until RNA extraction was performed using the mirVana Kit (Ambion, cat. no. AM1560) according to the manufacturer's instructions. After DNase treatment followed by purification of mRNA via ethanol precipitation, the RNA quality was checked using electrophoresis (Agilent 1450 TapeStation).

Macrophage library preparation and sequencing

RNA-seq libraries were prepared using the MARS-seq protocol, as described previously.[83] Briefly, mRNA from cells was converted to cDNA alongside sample barcoding. Samples were pooled followed by second DNA strand synthesis and T7 *in vitro* transcription. Amplified RNA was fragmented, followed by ligation of partial P5 Illumina sequence and converted to cDNA. Full sequences of P5 and barcoded P7 were added by PCR. Libraries were prepared and sequenced on an Illumina instrument to a depth of 0.8–2.6 million reads per sample.

Macrophage read processing and mapping statistics

Sequencing reads were filtered, demultiplexed, and mapped to the human genome (hg19), using the MARS-seq analysis pipeline, as described previously.[83] Data were normalized to a library size factor. Factors were calculated by dividing the total number of reads from each sample to the median of the total number of reads across all samples. Data were transformed to a $\log_2$ scale. A minimal expression threshold was set to 3.5. One sample was removed from the dataset due to low read coverage.

Macrophage differential gene expression analysis

Statistical analysis was performed using a one-way ANOVA. False discovery rate (FDR) was used to account for multiple testing. Genes with an adjusted $p < 0.1$ were considered significantly differentially expressed. Genes were classified as upregulated based on their expression changes between infected samples and naive samples.

Purification of TcpF, MshA and sfGFP

The proteins TcpF, MshA and GFP were purified via affinity chromatography using Protino Ni-IDA Resin (Macherey-Nagel, cat. No. 745210.120). *E. coli* BL21 (DE3) Star was transformed with a pET plasmid containing *tcpF*, *mshA* or *sfgfp* with a C-terminal 6x-His-Tag. The cells were grown over night at 30°C in the presence of 0.05% lactose for protein expression. After cell lysis by sonication, proteins were purified according the manufacturer's protocol. Successful protein purification was verified by SDS-PAGE.[84]

Sample preparation for liquid chromatography-mass spectrometry (LC-MS) analysis

To identify the binding partner of MshA and TcpF on the surface of macrophages or to investigate differential protein abundance between macrophages and monocytes, $3x10^6$ THP-1 monocytes were differentiated into macrophages using culture dishes with a diameter of 60 mm as described above. Macrophages were washed three times with 5 mL PBS (pH 7.5). Afterward, a total of 6 mL of ice-cold lysis buffer was added (for MshA and TcpF experiments: 50 mM Tris, 150 mM NaCl, 5% glycerol, 0.5% NP40, pH 7.5; for differential protein abundance experiment: 1% sodium deoxycholate, 10 mM TCEP, 100 mM Tris, pH = 8.5). Subsequently, macrophages were scraped off the surface and collected. Lysis of macrophages was achieved by vigorous pipetting every 5 min for a total time of 30 min on ice, followed by the usage of a tissue grinder. THP-1 monocytes ($3x10^6$ cells) were collected by centrifugation (200 g, 5 min) for each experiment and washed three times with 5 mL PBS. After the last washing step, monocytes were lysed in lysis buffer as described above. Lysates from macrophages and monocytes were stored at −80°C until further use.

For pulldown experiments, Protino Ni-IDA 150 columns were used (Macherey-Nagel, cat. no. 745150.10) and all steps were performed at 4°C. After equilibrating the column according to the manufacturer's protocol, the column was loaded with 1 mg of the purified 6x-His tagged bait protein (MshA, TcpF or GFP). After 30 min of incubation the column was drained by gravity. Subsequently, the lysate from macrophages or monocytes was loaded onto the column. After the cell lysate passed through, the column was washed five times with 500 μL LEW buffer containing 40 mM imidazole. Finally, bound proteins were eluted three times with 240 μL LEW buffer containing 250 mM imidazole and precipitated with 100% TCA (Sigma, cat. no. T6399). The pellet was washed with acetone and the proteins were dissolved in resuspension buffer (5% SDS, 10 mM TCEP, 100 mM TEAB).

For differential abundance measurements, monocyte and macrophage lysates were sonicated using a BioRuptor system (Diagenode, 10 cycles, 30 s ON, 30 s OFF).

The protein concentration in all samples was determined by tryptophan fluorescence analysis[85] using a small sample aliquot. Sample aliquots containing 50 μg of total proteins were reduced for 10 min at 95°C and alkylated at 15 mM chloroacetamide at 37°C for 30 min. Proteins were digested by incubation with sequencing-grade modified trypsin (1/50, w/w; Promega, Madison, Wisconsin) at 37°C for 12 h. Peptides were desalted using iST cartridges (Pre-Omics, Munich) according to the manufacturer's protocol. Samples were dried under vacuum and stored at −20°C until further use for LC-MS analysis.

Liquid chromatography-mass spectrometry (LC-MS) analysis

Dried peptide samples were dissolved in aqueous 0.1% formic acid solution and 0.15 μg of peptides were LC-MS analyzed as described previously.[86]

For differential protein abundance analysis of macrophages and monocytes, chromatographic separation of peptides was carried out using an Ultimate 3000 nano-LC (Thermo Fisher Scientific), equipped with a heated RP-HPLC column (75 μm × 30 cm) packed in-house with 1.9 μm C18 resin (Reprosil-AQ Pur, Dr. Maisch). Peptides were analyzed per LC-MS/MS run using a stepwise linear gradient ranging from 98% solvent A (0.15% formic acid, 2% acetonitrile) and 2% solvent B (98% acetonitrile, 2% water, 0.15% formic acid) to 12% B over 5 min, followed by an increase to 35% B over 45 min, followed by an increase to 50% B for 10 min at a flow rate of 300 nL min^{-1}. Mass spectrometry analysis was performed on a Orbitrap Eclipse mass spectrometer equipped with a nano-electrospray ion source (both Thermo Fisher Scientific) using data-independent acquisition (DIA). For MS1, the Normalized AGC Target setting was set to 300% over a maximum injection time of 45 ms and scans were recorded at a resolution of 120,000 FWHM. DIA scans were acquired at a Normalized AGC Target setting of 400% at an accumulation time of 22 ms and resolution was set to 15,000 FWHM (at 200 *m/z*). A total of 70 DIA windows with size of 9 *m/z* covering a mass range from 386 to 1016 *m/z* with 1 *m/z* window overlap were collected per MS cycle. The HCD collision energy was set to 28% (normalized) and all data were acquired in centroid mode.

For affinity pulldown analysis with MshA, TcpF and GFP, peptides were subjected to LC-MS/MS analysis using a Q Exactive Plus mass spectrometer fitted with an EASY-nLC 1000 (both Thermo Fisher Scientific). Peptides were resolved using an EASY-Spray column (PepMap RSLC, C18, 2 μm, 100 A, 75 μm × 25 cm, Thermo Scientific) at a flow rate of 200 nL min^{-1}. A stepwise linear gradient ranging from 5% buffer B to 10% buffer B over 5 min, followed by an increase to 35% buffer B over 30 min, followed by an increase of buffer B to 50% in 5 min was used for peptide separation. Buffer A consisted of 0.1% formic acid in water and buffer B consisted of 80% acetonitrile, 0.1% formic acid in water. The mass spectrometer was operated in DDA mode with a total cycle time of approximately 1 s. Each MS1 scan was followed by high-collision-dissociation (HCD) of the 20 most abundant precursor ions with dynamic exclusion set to 30 s. For MS1, $3x10^6$ ions were accumulated in the Orbitrap over a maximum time of 100 ms and scanned at a resolution of 70,000 FWHM (at 200 *m/z*). MS2 scans were acquired at a target setting of $1x10^5$ ions at a maximum accumulation time of 50 ms and a resolution of 17,500 FWHM (at 200 *m/z*). Singly charged ions, ions with charge state ≥ 6, and ions with unassigned charge state were excluded from triggering MS2 events. The normalized collision energy was set to 27%, the mass isolation window was set to 1.4 *m/z* and one microscan was acquired for each spectrum.

Mass spectrometry (MS) data analysis

For differential protein abundance analysis of macrophages and monocytes, the acquired raw-files were searched by directDIA against the human UniProt protein database (version Feb 2022) and commonly observed contaminants (in total 20,753 sequences) by the SpectroNaut software (Biognosys, version 15.7.220308.50606) using default settings. The search criteria were set as follows: full tryptic specificity was required (cleavage after lysine or arginine residues unless followed by proline), 2 missed cleavages were allowed, carbamidomethylation (C) was set as fixed modification and oxidation (M) and N-terminal acetylation as a variable modification. The false identification rate was set to 1%. The search results were exported from SpectroNaut and protein abundances were statistically analyzed using MSstats (v.4.2.0).[75] In order to identify proteins that are associated with the surface of macrophages from all differentially abundant proteins (fold change >2, p value < 0.05), the data was filtered for the subcellular location using the following Gene Ontology terms: cell surface, extracellular region, extracellular exosome, extracellular space, external side of plasma membrane, apical plasma membrane using DAVID.[87,88] In addition, we searched for proteins with the UniProt Annotation "secreted".

For affinity pulldown analysis with MshA, TcpF and GFP, the acquired raw-files were searched by FragPipe using MSFragger[89] against the human UniProt protein database (version Feb 2022) containing the predicted UniProt entries of TcpF and MshA from *V. cholerae* N16961 (EBI, release date 2022/5/12) and commonly observed contaminants (in total 20,755 sequences). Default settings were used for search, and search criteria were set as follows: full tryptic specificity was required (cleavage after lysine or arginine residues unless followed by proline), 2 missed cleavages were allowed, carbamidomethylation (C) was set as fixed modification and oxidation (M) and N-terminal acetylation as a variable modification. A target-decoy search strategy was used in order to obtain a protein false discovery rate of 1%. Search results were analyzed using the Scaffold software environment (https://www.proteomesoftware.com). In order to identify proteins that are associated with the surface of macrophages from all enriched proteins in the pulldown experiments, the data was filtered for the subcellular location using the following Gene Ontology terms: cell surface, extracellular region, extracellular exosome, extracellular space, external side of plasma membrane, apical plasma membrane. In addition, we searched for proteins with the UniProt Annotation "secreted". In case of the affinity pulldown analysis for MshA, the list of potential eukaryotic binding partners was further filtered for proteins that showed a fold change >2 and a p value < 0.05 in our differential abundance analysis using macrophages and monocytes.

Image analysis

Image analysis was based on the BiofilmQ software tool[90] using the MATLAB environment, as well as MATLAB scripts for the macrophage detection and biofilm abundance measurements. Image segmentation was performed using traditional filtering and thresholding operations, as reviewed recently,[91] without machine learning-based segmentation. Specific image analysis strategies for particular quantifications are described below.

Macrophages were detected in the images by median filtering the raw image for noise removal. This was followed by thresholding with Otsu's method applied to a strongly blurred image using three classes, where the second class was assigned to be the foreground.[92] Regions in the image where bacterial cells were present were excluded to avoid false-positives due to a small overlap between the fluorescence channels. After thresholding, morphological operations were performed to remove small objects and remove holes in the detected macrophage image regions, and the outlines of macrophages were smoothed.

For the detection of dead macrophages, confocal fluorescence images of the dead stain channel (dead stain: propidium iodide) were median-filtered to remove noise, followed by thresholding. Depending on the image quality, the threshold was set to the mean of the two thresholds determined by Otsu's method with three classes, or calculated at the mean plus seven times the standard deviation of a normal distribution fitted to the 99.5% lowest pixel values in the image. The latter method provided more accurate segmentation results for images in which there were few or no dead macrophages. Morphological operations were then applied to the resulting binary image to remove very small binary objects. The resulting number of dead macrophages was then determined by overlapping the binary image from the dead cell fluorescence channel with the macrophage detection (described above) and counting the number of macrophages that contained a signal in the dead cell fluorescence channel. To obtain the ratio of dead cells, the number of dead macrophages was divided by the number of all macrophages, which was corrected by counting macrophages that were touching (which were segmented as a single large object) as several macrophages, depending on their size in relation to the typical size of a macrophage.

For the quantification of the volume of attached bacterial cells per volume around the macrophages, image segmentation was performed using Otsu thresholding followed by a removal of very small segmentation objects resulting from noise. For each 2D image in the confocal image z stack, all image areas occupied by bacteria which were connected to a macrophage object in the image after image dilation by 4 pixels (corresponding to 1.3 μm) were defined to be attached to a macrophage. All connected image areas occupied by bacteria in an annulus around a macrophage object were summed up and separately the area of the annulus around the macrophage was calculated. The thickness of the annulus was set to 3 μm when only a few bacteria attached to immune cells and attachment was quantified from confocal images that were taken 0.5 h or 1 h after start of the experiment. In case biofilm formation was investigated for several hours and all images from the time-series were analyzed, the thickness of the annulus was set to 6 μm for all frames. After calculating the volume of attached bacteria per volume around macrophages and the volume of the annulus for three xy-slices of the z stack, the ratio of volumes from all slices were averaged to result in the volume of attached bacteria per volume of the annulus around each macrophage. This quantification was performed for all macrophages in the field of view.

For the quantification of biofilm matrix abundance in images in Figures 3B–3D, bacterial cells and matrix were segmented using thresholding in their separate fluorescence channels. The binary image representing locations of bacteria and the binary image representing the matrix were then merged, using the ''merge channels'' functionality of BiofilmQ, yielding a segmentation of the entire biofilm biovolume. These binary images were the basis for biofilm matrix abundance quantifications.

To quantify the abundance of hemolysin around macrophages, images of detected hemolysin (via fluorescent antibodies) and macrophages were segmented using Otsu thresholding. Subsequently, the volume occupied by hemolysin was measured within a volume with a distance of 7 μm to each detected macrophage surface.

The architecture of biofilms was analyzed at the single-cell level, by first performing a 3D cellular segmentation using an algorithm described previously.[26] The binary images resulting from the single-cell segmentation were then imported into BiofilmQ for downstream quantifications. Using this approach, we determined the local cellular alignment around each cell (quantified as the nematic order parameter), the local cell-cell distance (quantified as cell-center to cell-center distance), as well as local cell density inside the biofilm. All of these properties were quantified locally, in a sphere of radius 45 pixels (2.9 μm) around each cell, for all cells in the biofilm.

Schematic diagrams

Schematic diagrams in Figures 6, S5, and S6, and the graphical abstract were created with BioRender.com.

QUANTIFICATION AND STATISTICAL ANALYSIS

Statistical analysis was performed using Prism (GraphPad Software Inc.). Statistical details of experiments can be found in figure legends.

CellPress
OPEN ACCESS

Supplemental figures

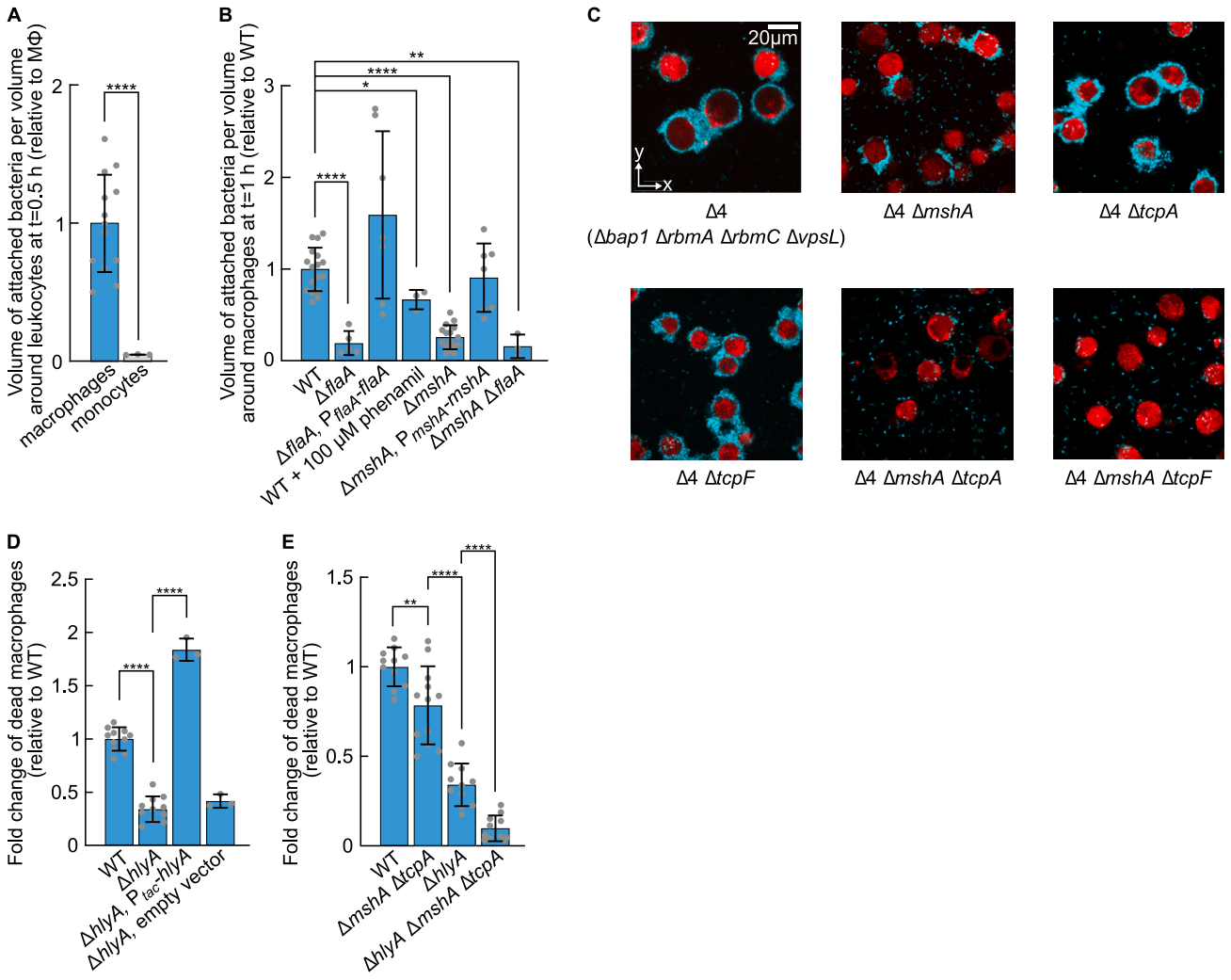

Figure S1. Colonization and death of macrophages differentiated from CD14⁺ monocytes isolated from human blood by *V. cholerae*, and attachment of bacteria to primary CD14⁺ monocytes, refers to Figures 1, 2, 3, and 5

(A) *V. cholerae* WT exhibits strongly reduced attachment to CD14⁺ monocytes compared with macrophages (Mφ) derived from CD14⁺ monocytes. Attachment of *V. cholerae* to immune cells was quantified from confocal images after 0.5 h of co-incubation and normalized to the mean value for macrophages. Statistical significance was calculated using an unpaired t test (number of independent biological replicates: $n_{macrophage} = 12$, $n_{monocyte} = 3$; **** indicates $p < 0.0001$). Error bars denote the standard deviation.

(B) Attachment capabilities of different *V. cholerae* strains to the surface of macrophages derived from CD14⁺ monocytes normalized to the mean value of WT bacteria. For bacteria with a stalled flagellar motor (achieved by the addition of phenamil), cells that lack the polar flagellum (Δ*flaA*), or cells lacking MSHA pili (Δ*mshA*), attachment to macrophages is attenuated. Ectopic expression of *mshA* or *flaA* under control of the native promoter restores bacterial attachment. Statistical significance was calculated using one-way ANOVA (number of independent biological replicates: n = 3–16; * indicates $p < 0.05$; ** indicates $p < 0.005$; **** indicates $p < 0.0001$). Error bars denote the standard deviation.

(C) Representative microscopy images from n = 3–8 independent biological replicates show *V. cholerae* biofilms (cyan) formed on primary macrophages (red) differentiated from CD14⁺ monocytes isolated from human blood, imaged at peak time of biofilm formation. The *V. cholerae* biofilm matrix components Bap1, RbmA, RbmC, and *Vibrio* polysaccharide (VPS) are not required for biofilm formation on human macrophages. Instead, *V. cholerae* biofilm formation on macrophages derived from CD14⁺ monocytes depends on the production of MSHA pili and TC pili (with the secreted protein TcpF).

(D) During co-incubation of macrophages with *V. cholerae* lacking hemolysin HlyA, macrophage death is significantly reduced compared with WT bacteria. Overexpression of *hlyA* under control of the inducible P_{tac} promoter restores and enhances bacteria-induced killing of macrophages. Macrophage death was

(legend continued on next page)

measured after 7 h of exposure to bacteria. Bars represent the percentage of dead macrophages for different *V. cholerae* strains, normalized to the WT mean value. Statistical significance was calculated using an unpaired t test (n = 3–11 independent biological replicates; **** indicates $p < 0.0001$). Error bars denote the standard deviation.

(E) Biofilm growth on macrophages supports hemolysin-dependent death of macrophages. During co-incubation, *V. cholerae* strains deficient in the formation of biofilms on macrophages (strains carrying the Δ*mshA* and Δ*tcpA* mutations) cause less death of macrophages compared with biofilm-capable bacteria. Bars represent the percentage of dead macrophages for different *V. cholerae* strains normalized to the WT. Macrophage death was measured after 7 h of exposure to bacteria. Statistical significance was calculated using an unpaired t test (n = 3–11 independent biological replicates; **** indicates $p < 0.0001$; ** indicates $p < 0.007$). Error bars denote the standard deviation.

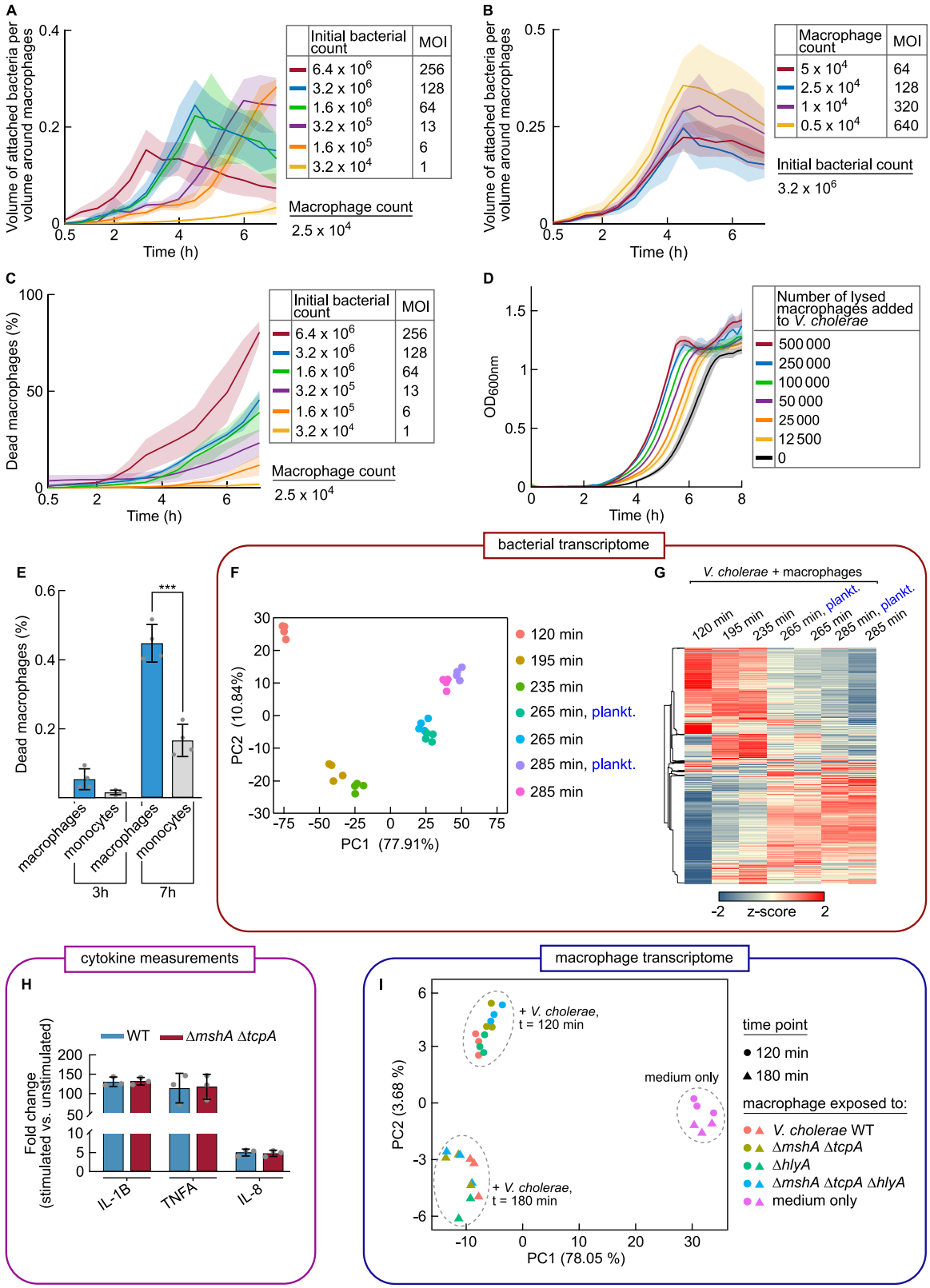

(legend on next page)

Figure S2. The impact of initial bacterial and macrophage counts on *V. cholerae* biofilm formation dynamics and macrophage death, the effect of macrophage lysate on *V. cholerae* growth, the effect of *V. cholerae* on monocyte death, and responses of *V. cholerae* and macrophages to each other during co-culture, refers to Figures 1 and 5

(A) Changing the number of bacterial cells added to a constant number of macrophages (2.5×10^4; in a well of a 96-well plate filled with 200 μL of medium) does not change the interaction outcome qualitatively but impacts the dynamics of biofilm growth and the time point of biofilm dispersal. A higher number of bacterial cells added to 2.5×10^4 macrophages at the beginning of co-incubation results in a faster biofilm formation on the surface of the immune cells. Lower bacterial seeding densities lead to longer lag times in biofilm formation. The different bacterial seeding densities correspond to an MOI at the start of infection in the range of 1–256. Lines represent the mean ratio of the volume of attached bacteria per volume of an annulus around each macrophage. Shaded areas indicate the standard deviation of n = 3 independent biological replicates.

(B) Changing the number of macrophages present inside a well of a 96-well plate, filled with 200 μL of medium containing initially 3.2×10^6 *V. cholerae* cells, does not change the biofilm formation process temporally. The different bacterial seeding densities correspond to an MOI at the start of infection in the range of 64–640. Lines denote the mean ratio of the volume of attached bacteria per volume of an annulus around each macrophage, and shaded areas are the standard deviation of n = 3 independent biological replicates.

(C) Changing the number of bacterial cells added to a constant number of macrophages (2.5×10^4; in a well of a 96-well plate filled with 200 μL of medium) strongly impacts the occurrence of macrophage death. A higher number of bacterial cells added at the beginning of co-incubation results in a higher percentage of dead macrophages after 7 h of co-incubation. Lines represent the mean of dead macrophages for different initial bacterial counts, and shaded areas represent the standard deviation of n = 3 independent biological replicates.

(D) Supplementation of growth medium with lysate from macrophages enhances bacterial growth by reducing the lag phase in a concentration-dependent manner. When the number of lysed macrophages that is added to a constant number of *V. cholerae* cells (3.2×10^6 cells, in a total volume of 200 μL) is increased, the bacterial cells reach exponential growth faster. The effect of lysed macrophages on the growth of *V. cholerae* was monitored with an automated plate reader at 37°C. Colored lines represent the mean OD_{600} values that reflect the *V. cholerae* cell density in the culture, and shaded areas represent the standard deviation of n = 4 independent biological replicates.

(E) Measurements of the fraction of dead macrophages and monocytes after 3 h and 7 h of co-incubation with *V. cholerae* WT cells. After 3 h of exposure to *V. cholerae*, the differences in the fraction of dead macrophages and monocytes are not statistically significant. After 7 h of co-incubation, the occurrence of dead immune cells is significantly increased for macrophages compared to monocytes. Statistical significance was calculated using an unpaired t test (n = 4 independent biological replicates; *** indicates p = 0.0002). Error bars denote the standard deviation.

(F) Principal-component analysis (PCA) of the bacterial RNA-seq data shows global changes in the bacterial transcriptome during the interaction with macrophages. In addition, the four biological replicates (dots with the same color) belonging to each sampled time point (indicated by different colors) cluster together. The PCA was performed based on fold change values that were calculated for each significantly differential expressed gene, relative to the average of all naive bacterial samples at 0 min (immediately prior to exposure to macrophages). Individual data points of n = 4 independent biological replicates are shown. Transcriptome data are available at the Gene Expression Omnibus (GEO: GSE184078).

(G) Clustering of the 3,519 *V. cholerae* genes (rows) shows significant changes in gene expression over the course of the interaction with macrophages (columns). The heatmap displays the *Z* score calculated from average fold change values for each gene and time point relative to the average of the naive bacterial sample at 0 min. Values are the mean of n = 4 independent biological replicates.

(H) ELISA measurements of cytokine abundance in supernatants show that biofilm formation of *V. cholerae* on the surface of macrophages does not prevent the release of IL-1B, TNFA, or IL-8 into the extracellular environment. The amount of IL-1B, TNFA, and IL-8 in the supernatant were similar for biofilm-producing bacteria (WT) and biofilm-deficient bacteria (Δ*mshA* Δ*tcpA*). However, the production of all three cytokines was significantly induced by co-culture with *V. cholerae* compared to unstimulated macrophages. Statistical significance was calculated using an unpaired t test (n = 3 independent biological replicates). Error bars denote the standard deviation.

(I) Macrophage transcriptomes display changes after exposure to *V. cholerae* as illustrated by the PCA. Transcriptomes were measured by RNA-seq. Bacteria deficient in biofilm formation or hemolysin production and WT bacteria induce similar transcriptional changes in macrophages. The PCA was performed on 296 significantly upregulated macrophage genes. Individual data points of n = 3 independent biological replicates are shown: each data point corresponds to a transcriptome; different time points are indicated by a dot or triangle, and each bacterial strain used for the interaction studies is indicated by a different color. Transcriptome data are available at the Gene Expression Omnibus (GEO: GSE184077).

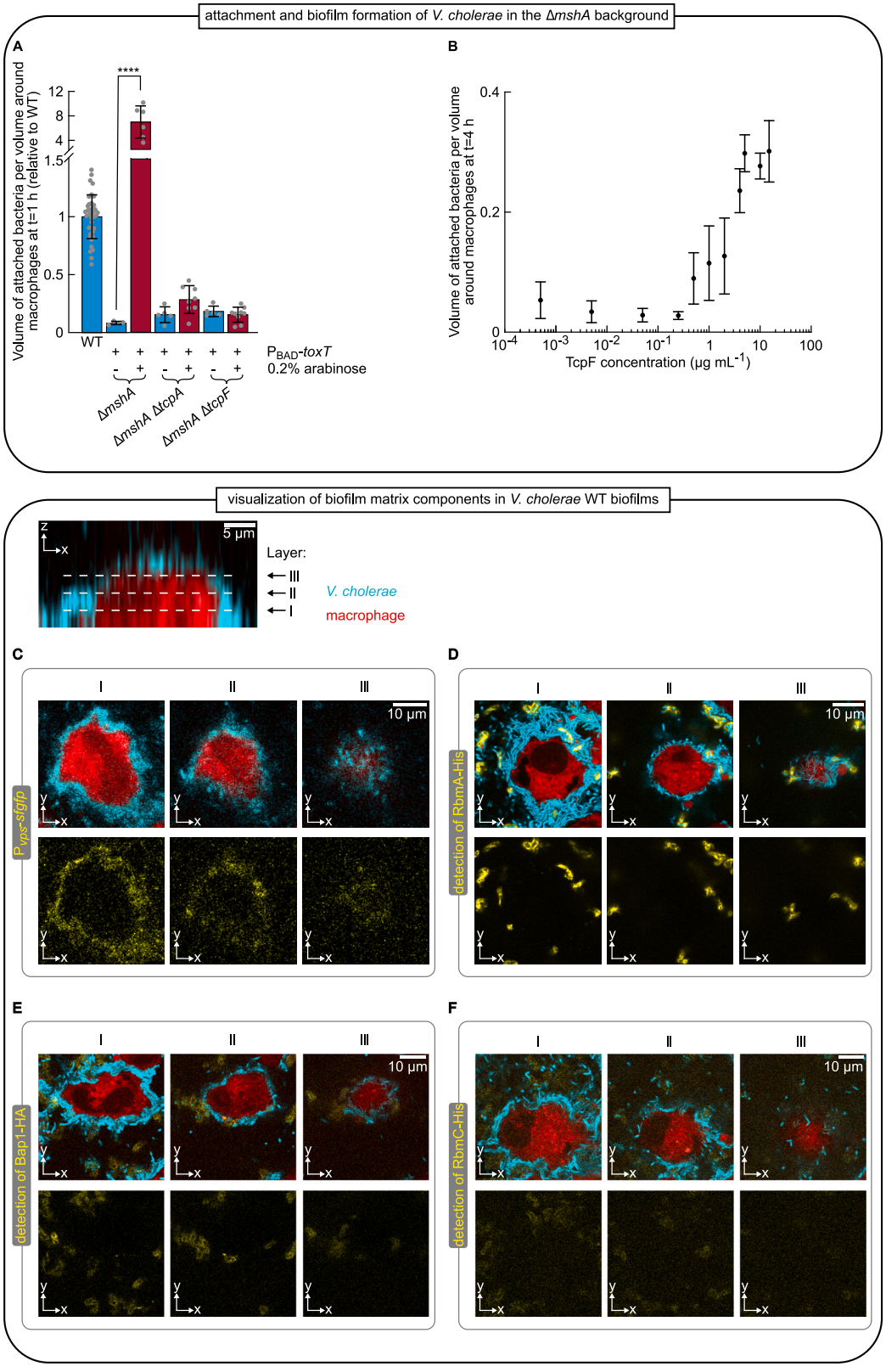

(legend on next page)

Figure S3. Impact of TC pili and TcpF on attachment and biofilm formation of Δ*mshA* cells and localization of RbmA, Bap1, and RbmC, as well as transcription of *vps* genes inside mature *V. cholerae* WT biofilms formed on macrophages, refers to Figures 2 and 3

(A and B) Overexpression of the *tcp* operon was achieved by placing *toxT* under the control of the arabinose inducible promoter P_{BAD}.

(A) The overexpression of the *tcp* operon, achieved by the addition of 0.2% arabinose, resulted in strong attachment of Δ*mshA* cells after only 1 h of co-incubation, which was dependent on the presence of TC pili and TcpF. Bars represent mean values, after normalization to the mean obtained for WT bacteria. Error bars denote the standard deviation of n independent biological replicates ($n_{\Delta mshA,\ 0\%} = 4$; $n_{\Delta mshA,\ 0.2\%} = 6$; $n_{\Delta mshA\ \Delta tcpA,\ 0\%} = 5$; $n_{\Delta mshA\ \Delta tcpA,\ 0.2\%} = 8$; $n_{\Delta mshA\ \Delta tcpF,\ 0\%} = 5$; $n_{\Delta mshA\ \Delta tcpF,\ 0.2\%} = 9$). Statistical significance was calculated using an unpaired t test (**** indicates $p < 0.002$).

(B) Overexpression of TC pili is not sufficient for biofilm formation on macrophages in a Δ*mshA* Δ*tcpF* strain. However, increasing the concentration of exogenously supplied purified TcpF enabled the Δ*mshA* Δ*tcpF* strain to form biofilms after 4 h of co-incubation. This indicates that TC pili interact with TcpF in order to bind to the macrophage surface, while secreted TcpF localizes on the macrophage surface (Figure 3D). For these experiments, we initiated the co-culture with 3.2×10^6 bacteria and 2.5×10^4 macrophages in 200 μL of culture medium. Dots denote the mean ratio of the volume of attached bacteria per volume of an annulus around each macrophage, and error bars represent the standard deviation of n = 4–10 independent biological replicates.

(C–F) Macrophages are shown in red, *V. cholerae* cells are shown in cyan, and immunofluorescence or reporter fluorescence is shown in yellow. Each panel shows xy planes at three different *z*-heights, indicated by the Roman numerals I–III. The Roman numerals in (A)–(D) refer to different *z*-height layers as indicated in the side view (xz plane) at the top of the figure. For each panel, representative confocal fluorescence microscopy images from n = 3–4 independent biological replicates are shown.

(C) The transcription of *vps* genes is measured via an sfGFP-based transcriptional reporter. Transcription of *vps* genes occurs throughout the biofilm formed on macrophages.

(D) Histidine (His)-tagged RbmA is detected extracellularly using a fluorescent anti-His antibody shown in yellow.

(E) Hemagglutinin (HA)-tagged Bap1 is detected extracellularly using a fluorescent anti-HA antibody shown in yellow.

(F) Histidine (His)-tagged RbmC is detected using a fluorescent anti-His antibody shown in yellow. (B)–(D) show that RbmA, Bap1, and RbmC are present around some bacterial cells that are part of biofilms on the macrophage surface. RbmA, Bap1, and RbmC encapsulate cells that are located at the outer edge of the biofilms and are not observed on bacterial cells that are closest to the macrophage surface.

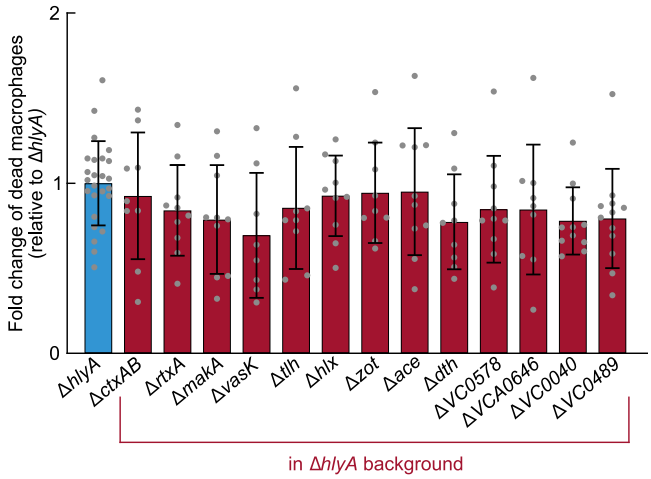

Figure S4. The toxin HlyA is primarily responsible for causing macrophage death, refers to Figure 5

The extent of cell death of THP-1-derived macrophages was determined after 7 h of co-incubation with *V. cholerae* strains carrying the Δ*hlyA* deletion and the deletion of one additional (putative) toxin. The results were normalized to the mean of the Δ*hlyA* strain. Compared with the Δ*hlyA* strain, *V. cholerae* deletion mutants lacking *hlyA* together with one additional gene encoding a known or putative toxin do not significantly alter the occurrence of macrophage death. Bars represent the mean values, and error bars denote the standard deviation. The changes in macrophage death for the different bacterial strains in comparison to Δ*hlyA* are not statistically significant. Statistical significance was calculated using one-way ANOVA (n = 9–25 independent biological replicates). Error bars denote the standard deviation.

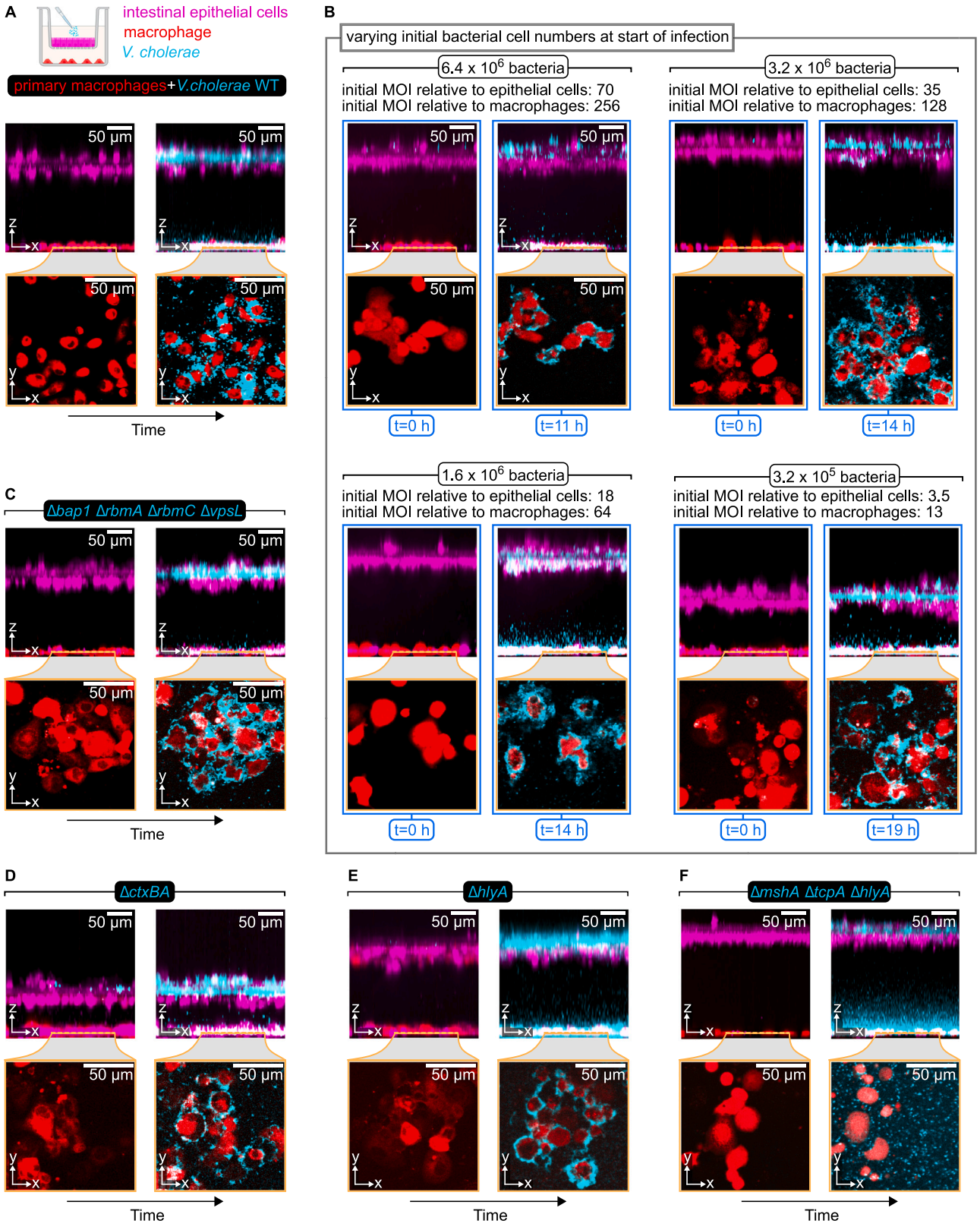

(legend on next page)

Figure S5. Infection of the enteroid-macrophage co-culture model with *V. cholerae* for different MOIs, different bacterial mutants, and different macrophages, refers to Figure 6

(A) A confluent intestinal epithelial monolayer comprising 9.1×10^4 cells was grown from human enteroids (donor #1) on a permeable membrane insert (3 μm pore size) and placed above 8×10^4 macrophages that were differentiated from primary monocytes obtained from human blood. After adding 3.2×10^6 *V. cholerae* WT cells, the co-culture dynamics resembled the ones observed for THP-1 macrophages shown in Figure 6A. Representative confocal fluorescence microscopy images of n = 3 independent biological replicates show the xz side view (maximum projection) at the start of the co-culture and at the time of peak biofilm formation on primary macrophages (magenta: epithelial cells, red: macrophages, cyan: *V. cholerae*). For the same time points, xy images show macrophages and *V. cholerae* biofilms underneath the epithelial cells.

(B) Co-culture of intestinal epithelial monolayers grown from enteroids (donor #1) on a membrane insert with 3 μm pore size and THP-1 macrophages, which was inoculated with varying numbers of *V. cholerae* WT cells (for 9.1×10^4 epithelial cells, 2.5×10^4 THP-1 macrophages). Higher bacterial cell numbers at the start of infection resulted in an earlier crossing of the epithelial barrier and biofilm formation on macrophages. Representative fluorescence images of n = 3 independent biological replicates show the xz side view (maximum projection) of enteroid monolayers, macrophages, and bacteria at the start of the co-culture and at the time of peak biofilm formation on macrophages. For the same time points, xy images show macrophages and *V. cholerae* biofilms underneath the epithelial cells.

(C–F) Co-culture of confluent intestinal epithelial monolayers grown from enteroids (donor #1) on a membrane insert with 3 μm pore size with THP-1-derived macrophages and different *V. cholerae* deletion mutants (mutations are indicated above each panel). Cell numbers at the start of infection: 3.2×10^6 bacteria, 9.1×10^4 epithelial cells, and 2.5×10^4 THP-1 macrophages. Representative confocal fluorescence microscopy images of n = 3 independent biological replicates for each mutant show xz side views (maximum projection) and xy images in the same format as for (A). (C)–(E) show that *V. cholerae* impaired in the production of the known biofilm matrix components Bap1, RbmA, RbmC, and VPS as well as cells lacking cholera toxin (Δ*ctxBA*) or hemolysin (Δ*hlyA*) accumulated on the apical side of monolayers, crossed the epithelial barrier, and formed biofilms on the surface of the underlying macrophages, similar to the WT. Microscopy images show the bacterial interaction with enteroid monolayers and macrophages at the start of co-culture and the time of peak biofilm formation on macrophages. (F) shows *V. cholerae* deficient in the production of MSHA pili, TC pili, and hemolysin (Δ*mshA* Δ*tcpA* Δ*hlyA*) were unable to form biofilms on the surface of macrophages after crossing the epithelial barrier. Microscopy images show the start of the experiment and a time point when the WT would have formed biofilms.

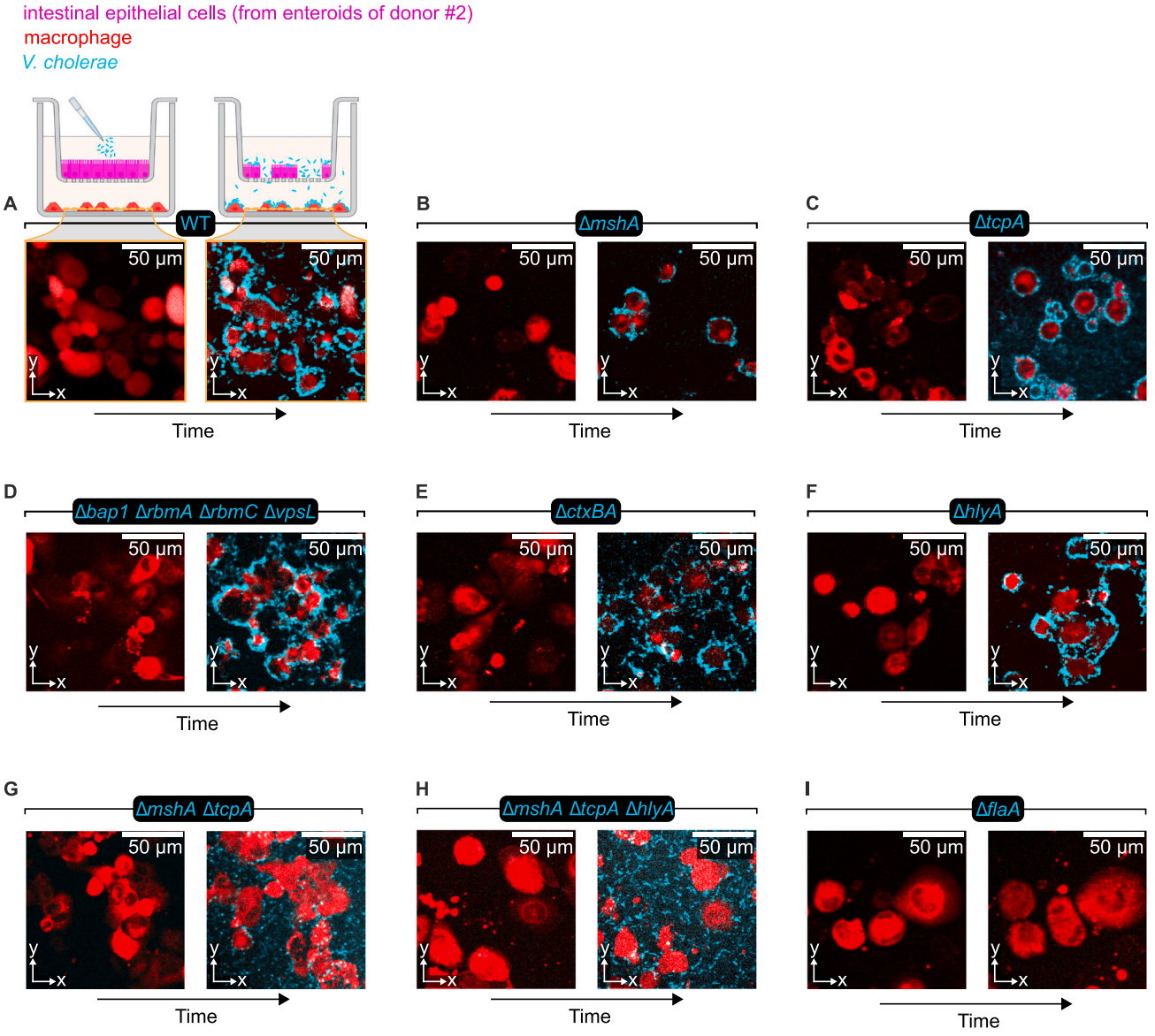

Figure S6. Co-culture results of different *V. cholerae* strains with THP-1 macrophages and human enteroid monolayers from donor #2, refers to Figure 6

These results are analogous to those shown in Figures 6A and 6C–6F but using a confluent intestinal epithelial monolayer that was generated from enteroids of donor #2. The human enteroid monolayer was grown on a permeable membrane insert (3 μm pore size) and placed above THP-1 macrophages as illustrated in the schematic diagram of the experimental setup (magenta: epithelial cells, red: macrophages, cyan: *V. cholerae*). Representative confocal fluorescence microscopy images of n = 3 independent biological replicates are shown for each bacterial strain. Cell numbers at the start of infection: 3.2 × 10^6 bacteria, 31 × 10^4 epithelial cells, and 2.5 × 10^4 THP-1 macrophages.

(A–F) *V. cholerae* WT cells and bacteria lacking MSHA pili (Δ*mshA*) or TC pili (Δ*tcpA*) formed biofilms on the surface of macrophages after crossing the epithelial barrier. Similarly, biofilm formation on macrophages was observed for bacteria that cannot produce the biofilm matrix components RbmA, RbmC, Bap1, and VPS (Δ*bap1* Δ*rbmA* Δ*rbmC* Δ*vpsL*) and bacteria that cannot produce the cholera toxin (Δ*ctxBA*) or hemolysin (Δ*hlyA*). Images show the xy plane at the start of the co-culture and at peak time of biofilm formation on macrophages.

(G–H) Bacterial strains that cannot produce MSHA pili and TC pili (Δ*mshA* Δ*tcpA* or Δ*mshA* Δ*tcpA* Δ*hlyA*) were unable to form biofilms on macrophages after breaching the epithelial barrier. Images show the xy plane at the start of the co-culture and a time point when WT bacteria would have formed biofilms on macrophages.

(I) Non-motile bacteria (Δ*flaA*) could not break through the epithelial barrier, and Δ*flaA* mutants were consequently not observed at the basal side of enteroid monolayers. Microscopy images show the start of the experiment and a time point when WT bacteria would have formed biofilms on macrophages.